ABSTRACT

Title of Thesis:	QUANTIFYING NITROGEN REMOVAL POTENTIAL OF BOTTOM CAGE (*C. VIRGINICA*) AQUACULTURE
	Stefenie Shenoy, Master of Science, 2022
Thesis Directed By:	Professors Lora Harris, Jeremy Testa Marine-Estuarine-Environmental Science University of Maryland Center for Environmental Science Chesapeake Biological Laboratory

While management strategies for human-caused nutrient pollution have improved over the last decade, eutrophication and its ecological effects remain primary concerns in many coastal marine systems. In-water nutrient removal techniques are being explored for potential use as a management strategy, including oyster aquaculture operations. Where abundant, oysters have been shown to exhibit denitrifying potential beyond that which is assimilated into shell and tissue biomass. While nitrogen cycling dynamics are well studied and modeled on natural and restored reefs, equivalent processes within oyster aquaculture operations are less defined. This study adapts an existing mechanistic model of oyster filtration, biodeposition, and particle transport to capture the influence of an aquaculture farm on local sediment-water chemical fluxes. Modifications included (1) revising the spatial domain to represent an array of bottom cages, and (2) integrating an existing bioenergetics module to mechanistically couple simulated seston removal from the water column via filtration and subsequent biodeposition by simulating oyster growth. Model simulations included a variety of oyster densities, farm sizes, natural reef, and no oyster scenarios. Two seasonal sampling campaigns of a bottom cage aquaculture site provided model forcing and validation data. Model output revealed complex relationships among oyster density and distribution, farm size, oyster growth and biodeposition. The estimated rates of net nitrogen removal suggest increased potential for oyster aquaculture operations to receive credits above what is currently being realized, and the calculations of such removal for management purposes should consider lease-specific configurations and environmental parameters.

QUANTIFYING NITROGEN REMOVAL POTENTIAL OF BOTTOM CAGE (*C. VIRGINICA*) AQUACULTURE

by

Stefenie Shenoy

Thesis submitted to the Faculty of the Graduate School of the
University of Maryland, College Park, in partial fulfillment
of the requirements for the degree of
Master of Science
2022

Advisory Committee:
  Dr. Lora Harris, Co-Chair
  Dr. Jeremy Testa, Co-Chair
  Dr. Lawrence Sanford

© Copyright by
Stefenie Shenoy
2022

Acknowledgements

I am incredibly grateful to the members of my committee for their continued support and guidance: Dr. Lora Harris; Dr. Jeremy Testa; and Dr. Larry Sanford.

I would also like to acknowledge the support of my labmates and all those I have had the pleasure to work with over the course of the past two years. In particular, I am incredibly grateful to Casey Hodgkins and Isabel Sanchez, who immediately welcomed me to the CBL community and helped me to navigate graduate school in the virtual world.

To the friends that I have made along the way and those who started this journey with me, thank you for your sincerity, patience, and humor.

Finally, I thank my family for their endless support and love.

Table of Contents

List of Tables

List of Figures

Figure 19. Oyster growth rate (mgDW d^{-1}) averaged over time across a subsection of model domain where growth rate on the high-density farm becomes negative for some oysters within a cage (begining ~35 m into the farm). The small farm is not included because is was 35 m long. Due to the spatial partitioning of the advection-diffusion and oyster bioenergetic subdomains, the size of a cell changes with reef/farm length. This figure shows ~450 cells representing 6 cages plus the spacing in between them. Because each cell ranges from ~2.3-2.9 cm in length, this figure shows a section of farm/reef approximately 10.4 to 13.05 m in length, depending on the simulation.. The reef is the only simulation with a continuous array of oysters, seen here a continuous function.

Figure 20. Final shell length of an oyster across a subsection of model domain begining at the leading edge of the farm/reef. Due to the spatial partitioning of the advection-diffusion and oyster bioenergetic subdomains, the size of a cell changes with reef/farm length. This figure shows 475 cells representing 7 cages and the spacing in between them. Because each cell ranges from ~2.3-2.9 cm in length, this figure shows the first 11.0 to 13.78 m of farm/reef, approximately, depending on the simulation. The reef is the only simulation with a continuous array of oysters, seen here a continuous function.

Figure 21. Comparison of biodeposit export during all farm simulations. Resuspension occurred in 55% of timesteps for all farm scenarios.

Figure 22. Comparison of biodeposit export between the large farm and reef simulation. Resuspension occurred in 55% of timesteps during the farm simulation and 76% of timesteps during the reef simulation.

Figure 23. Total modelled biodeposit production (kg N) compared against biodeposit production calculated with the previous iteration of ReefBioDES (Jordan, 1987). Total deposition was calculated as the sum of biodeposits produced across the farm at each time step and then converted to grams of N using the same model conversion factors of 4.8 mg N per g biodeposits (Jordan, 1987). Percent difference between the two outputs is given for each simulation.

Figure 24. Along farm average biodeposition rates (g N gDW^{-1} h^{-1}) for each simulation. A mid-farm section approximately 6 cages in length is shown, where values were averaged over the duration of the simulations. Due to the spatial partitioning of the advection-diffusion and oyster bioenergetic subdomains, the size of a cell changes with reef/farm length. This figure shows 375 cells representing 5 cages plus the spacing in between them. Because each cell ranges from ~2.3-2.9 cm in length, this figure shows a section of farm/reef approximately 8.62 to 10.88 m in length. The reef is the only simulation with a continuous array of oysters, seen here a continuous function.

Figure 25. Trends of biodeposition (g N) averaged across the farm and summed for each week (top) biodeposit production using model formulations and (bottom) comparison of mean biodeposit production of all simulation using model formulation compared to using the Jordan (1987) formulation.

Figure 26. Sediment-water nitrogen fluxes for all simulations plotted with the reference no-oyster scenario for ammonium (top) and nitrate (bottom) fluxes (µmol m^{-2} h^{-1}). Note that the daily rates are almost identical for the small farm and low-density scenarios .

Figure 27. Denitrification rates (µmol m^{-2} h^{-1}) of all simulations plotted with the reference no-oyster scenario. Note that the daily rates are almost identical for the small farm and low-density scenarios .

Figure 28. Grams of nitrogen removed via denitrification, burial, and tissue and shell accretion during the duration of the simulations (5 months). Tissue and shell N values were calculated only for the biomass that was acrued during the simulation.

Figure 29. Ammonium recycling efficiencies (top) and denitrification efficiencies (bottom) for each day of the simulation.

Chapter 1

Introduction

Mitigating pollution in the Chesapeake Bay with nutrient trading

Eutrophication and its ecological effects remain primary concerns in many coastal marine systems. First order symptoms of a nutrient enriched system include an overabundance of phytoplankton, toxic algae blooms, and hypoxia and anoxia (Glibert et al., 2005), all of which can lead to loss of aquatic vegetation (Boyd, 2020), reduced fisheries productivity (Conley et al., 2009) (Conley et al. 2009), and ecosystem collapse (Diaz & Rosenberg, 2008; Kemp et al., 2005). In the Chesapeake Bay region, eutrophication is primarily attributed to long-term increases in nitrogen (N) and phosphorus (P) loading (Hagy et al., 2004; Kemp et al., 2005), Agriculture and stormwater runoff, wastewater treatment plant (WWTP) effluent, and atmospheric deposition are the primary vectors of terrestrial derived N input. Management strategies have primarily focused on reducing nutrient loading by setting limits for these point and non-point sources of pollution. Such policies include the Environmental Protection Agency's (establishment of a Total Daily Maximum Load (TMDL) for N, P, and sediment entering the Chesapeake Bay watershed. This federally mandated, Bay-wide policy has driven improvements in Bay health by encouraging updates in WWTP technology, changes to stormwater systems, and setting nutrient loading reduction goals; however, these methods are often expensive and fail to address non-point sources of pollution. Such challenges in mitigating nutrient pollution have driven the advancements of novel in-water removal methods which can complement N and P load reduction efforts.

Nutrient credit trading has emerged as a practical, market-based strategy to meet TMDLs. Implementation of a trading program requires that nutrient sources are allotted target values of permitted nutrient loading. Credits are generated when sources reduce nutrient loading below their individual load allotments (Jones et al., 2010). Sources that have exceeded their individual load allotments can purchase nutrient credits to offset excess pollution. These credits provide buyers with an affordable way to meet their allotted pollution budgets while incentivizing credit generators to further reduce their loading (Stephenson & Shabman, 2017b). Alternatively, credits can be generated by in-water nutrient removal methods such as wetland construction and oyster aquaculture. The role of oyster aquaculture in water quality trading programs is starting to be defined, but is still in need of more articulation and development (Stephenson & Shabman, 2017b).

Granting nitrogen credits for the harvest of bivalve biomass from aquaculture operations has been recognized as a best management practice (BMP) and is approved in Virginia and Maryland (Cornwell et al., 2016). Unlike finfish aquaculture, which is sustained through supplementary nutrient inputs, oyster aquaculture utilizes nutrients readily available in the environment without the need for a supplemental food source. Oysters ingest organic matter from the water column and use it to build shell, somatic tissue, and, in diploid oysters, gonads, thereby removing organic nitrogen from the environment. Standardized formulas have been established to convert oyster harvest into nutrient trading credits. These methods approximate the pounds of N or P removed per tissue biomass of harvested oysters using an empirical formula derived from local data. In the case of *C. virginica*, shell and tissue N values tend to remain consistent enough across sites that crediting for tissue bioextraction is possible (Cornwell et al., 2016). Any N removed by oyster harvest is considered excess that can be quantified relatively easily and sold for credit within the constraints of crediting legislation. N removal via shell is not considered when allocating nitrogen credit because, ideally, harvested shells would be recycled back into the system as habitat for spat (i.e., juvenile oysters). As regional farming practices expand, there is increased potential for growers to engage in nutrient credit trading.

Oyster practices in the Chesapeake Bay

Globally, harvest from oyster aquaculture has surpassed that of public fisheries every year since 1952 (FAO, 2020). While public fishery production still exceeds private harvest in many areas of the Chesapeake Bay, the landscape of the oyster aquaculture industry is rapidly changing. In Maryland, oyster aquaculture production grew from representing only 1% of regional harvest in 2012 to 43% in 2019 (Van Senten et al., 2019). In Virginia, the two commercial sectors have been about equally as productive since 2015. There are a wide range of oyster practices in the Chesapeake Bay which, broadly, fall into one of three categories: restoration, public harvest, and private aquaculture. Reef restoration efforts can be passive (excluding wild harvest activities) and/or intensive (adding substrate or planting hatchery produced oysters to increase populations). Aquaculture operations are generally classified as either extensive on-bottom culture, or intensive off-bottom farming. Growers may employ a single strategy or a combination of strategies over the lifespan of an oyster. Traditional, on-bottom culture of oysters is a comparatively less expensive practice where oyster culture is planted on a natural or artificially created bottom substrate and left to grow out in clusters which mimic the relatively flat topographic pattern of a natural or restored reef. Off-bottom culture refers to several diverse methodologies whereby clutchless oysters are grown out in containers such as trays, floating bags, or the bottom cages that are the focus of this study. These labor-intensive, and therefore relatively expensive, methods offer a more homogenous oyster product that is less susceptible to predation and other forms of mortality. Bottom cage cages may appeal to growers for the ability to rear more oysters per lease area compared to on-bottom culture. The definitions of and distinctions between these different practices are relevant in efforts to capture the complex interactions that oysters have with their environments, and how those interactions translate into different ecosystem services.

Ecosystem services associated with oyster communities

There is a growing body of research to suggest that expanding oyster aquaculture could garner benefits comparable to restored and natural reefs by way of supporting diverse ecological assemblages (Erbland & Ozbay, 2008; Marenghi et al., 2010; Mercaldo-Allen et al., 2021) mitigating cultural eutrophication (Ayvazian et al., 2021; M. L. Kellogg et al., 2014; Ray & Fulweiler, 2021). Encouraging oyster aquaculture, an already expanding industry in the Chesapeake Bay region, may also be an economically viable alternative to the high cost of restoring historic oyster reefs (Ray & Fulweiler, 2021; Stephenson & Shabman, 2017a, 2017b). Although oyster communities have demonstrated denitrifying potential beyond that which is assimilated into the shell and tissue biomass (Hoellein et al., 2015; Humphries et al., 2016; M. Kellogg et al., 2013; R. I. E. Newell et al., 2005), the inability to quantify this removal easily and reliably across diverse habitats prevents accurate crediting for this ecosystem service (Cornwell et al., 2016; M. Kellogg et al., 2013; Rose et al., 2021).

Mechanisms of oyster mediated nitrogen removal

Large oyster populations regulate N cycling through many processes. The three primary pathways of oyster mediated N removal that follow filter-feeding are 1) via sequestration into shell and tissue and eventual harvest, 2) through settling and subsequent burial of biodeposits in surrounding sediments, and 3) via enhancement of microbe driven, coupled nitrification-denitrification in the benthic community. The latter two are thought to result from the characteristic composition and behavior of oyster biodeposits and are the primary focus of this study. The aggregation of particulate organic matter (POM) into biodeposits has been shown to increase the likelihood of settling compared to unfiltered particles (Newell, 1996; Newell et al., 2005) while also providing the benthos with a source of detrital carbon (C) and N (Cranford et al., 2009).

Seston composition, hydrodynamics, and oyster biodeposition rates all influence the amount and composition of particulate organic nitrogen (PON) delivered to the benthos, which affects the subsequent cycling of nitrogen within the sediment and across the sediment-water interface (Tenore, 1988). Benthic microbial processes control the extent to which oyster-mediated deposition of organic material influences local biogeochemistry. For example, under oxygenated conditions, ammonium (NH_4^+) excreted by oysters or remineralized from organic matter can be oxidized to produce nitrite (NO_2^-) and nitrate (NO_3^-), which can then diffuse to anaerobic sediments for potential denitrification. In contrast, increased deposition of PON may stimulate respiration in the sediment microbial community, potentially reducing oxygen concentrations in the sediment (Mazouni et al., 1996) (Mazouzi et al. 1996). This in turn affects the nitrifying ability of aerobic microbes, effectively limiting coupled nitrification-denitrification.

The ongoing efforts to offer nitrogen credits to select aquaculture operations have revealed several gaps in knowledge that prevent nitrogen crediting schemes from encompassing the full potential of ecosystem services offered by oyster aquaculture. In 2015, the Chesapeake Bay Program commissioned the Oyster BMP Expert Panel to review existing literature on the capabilities of oysters to reduce suspended sediment and nitrogen and determine a method by which to capture those capabilities within a BMP. Based on available data and policy limitations, this initial review effort was constrained to consider only the nitrogen and phosphorus assimilation in oyster tissue (Cornwell et al., 2016). Several other types of crediting schemes were identified to be addressed in future discussions, including enhanced denitrification and N burial associated with private oyster aquaculture. In deciding not to make recommendations on the enhanced nutrient denitrification and burial rates created by oyster communities, the Panel cited 1) the variability in observational denitrification data and 2) the "complexity of quantifying" such enhancement. The focus of this thesis is to adapt an existing oyster reef model, "ReefBioDES", to an aquaculture setting, creating a fine-scale model that can be forced with site-specific environmental parameters and farm configurations.

Objectives

Modeling is a suitable approach to address the challenges identified in describing and quantifying oyster mediated N removal. Several studies have used modelling to predict and quantify the effect of large-scale oyster reef restoration on the health of the Chesapeake Bay (Cerco & Noel, 2007; Fulford et al., 2007);however, fine-scale dynamics of bottom cage oyster aquaculture are not well represented by current modeling efforts. The objective of this study was to apply a mechanistic model of oyster growth and biodeposition, sediment-water chemical fluxes, and oyster farm hydrodynamics known as Oyster Reef Filtration, Biodeposition, and Ecosystem Services (ReefBioDES) to model N cycling within bottom cage aquaculture. First, a bioenergetic model was added to mechanistically link filtration and biodeposition while also modeling oyster growth. Next, the hydrodynamic and biogeochemical conditions created by an array of aquaculture cages were captured with a modified spatial domain. Finally, delivery of biodeposits to a sediment-water chemical flux model (SFM) simulated benthic aerobic and anaerobic N transformations. These changes sought to describe and quantify the N removal potential of oysters in an aquaculture setting.

Nitrogen cycling is influenced by ambient temperature, total suspended solids (TSS) and chlorophyll concentration (food availability), and current velocity; environmental parameters that are expected to be different on a natural or restored reef compared to an aquaculture setting. These differences can be characterized by three major factors that were of particular interest in this modeling exercise: 1) bottom cages extend further up into the water column than bottom culture and restored or natural reefs. The hydrodynamic movement created by the addition of cages may block current flow or increase overall farm roughness to the point that flushing is limited (Duarte et al., 2014). 2) Increased roughness may slow boundary layer flow, reducing biodeposit resuspension and transport compared to a bare sediment surface (Reidenbach et al., 2013). 3) The density and size of oysters in an aquaculture setting may differ from that of a natural reef (e.g., 800 oysters per m^2 in aquaculture versus 50-200 oysters per m^2 in a restored reef). As a result of these three critical considerations, a shift in current flow, oyster density, nutrient availability, or any combination of these can affect the rates of N transformation on the farm. When placed in the context of existing nutrient management strategies and oyster aquaculture crediting, these considerations developed into the following primary research questions:

1. Is there an oyster density, farm length, or combination of the two at which food limitation negatively impact oyster growth?
2. How do aquaculture and restored reefs uniquely impact their environments, particularly in terms of N cycling?
3. What proportion of oyster mediated N removal is via indirect processes (enhanced denitrification and N burial) versus bioextraction (shell and tissue), and what factors influence these relative quantities?

These questions guided model development, constrained field sampling efforts to acquire forcing and validation data and informed a selection of simulations whose results could give insight into the often complex geophysical and biochemical dynamics of oyster assemblages and their environment.

Methods

Data collection at bottom cage aquaculture site

Forcing and validation data were obtained through multiple two-week observational campaigns at a bottom cage aquaculture lease located near the mouth of the Patuxent River. The farm was situated off the coast of Solomons Island, M.D. near Chesapeake Biological Laboratory (CBL). Sampling efforts included taking measurements of water quality parameters, hydrodynamic conditions, and particle distributions. An Acoustic Doppler Current Profiler (ADCP) collected current velocity data and water quality sondes (Xylem EXO2) collected data for chlorophyll-a, turbidity, water temperature, salinity, and dissolved oxygen measurements.

Each instrument collected data at 15 second intervals for the duration of the two-week deployments in the spring (April-May) and summer (July-August) in 2021. Three platforms with ADCPs and two platforms with YSI EXO2 sondes were deployed within and outside of the farm footprint (Fig. 1). One platform was located on the outside of the farm at the leading edge in the downstream direction at flood tide (ADCP+EXO2), one was located between the farm and the shoreline (ADCP only), and one near the middle of the farm (ADCP+EXO2). For model simulations, the outer platform on the leading edge of the farm was used as input data and the platform mid-farm was used for validation data.

Additionally, a tidal cycle survey was conducted in spring and summer 2021 to identify physical and biogeochemical trends across the farm (total suspended solids, chlorophyll-a, salinity, temperature). The primary sampling transect comprised of 7 sampling stations ran parallel to the shoreline and included three within-farm stations, one station NE of the farm, and three stations SW of the farm. An eighth sampling station was located shoreward of the farm outside the array of cages. (Fig. 1). The orientation of the primary sampling transect was chosen based on a pre-survey analysis of data available from a YSI EXO2 sonde at a long-term monitoring station near the farm (CBL Pier, 38.317 deg N, -76.450 deg W), which showed a dominant alongshore current velocity which was primarily SW at flood tide and NE at ebb. Surveys of each station were conducted at low, high, max-flood, and max-ebb tides. At each station, surface and bottom water samples were collected and filtered for total suspended solids (TSS) and chlorophyll-a (CHLA) using standard methods. Surface and bottom water measurements of dissolved oxygen, turbidity, water temperature, and salinity were collected using a YSI EXO2 sonde.

Model overview

The original version of ReefBioDES combined a fine-scale filtration and advection-diffusion oyster reef model (Ehrich & Harris, 2015), a biodeposit production and transport model (Kahover, 2022), and an adaptation of a sediment-water biogeochemical model (SFM) that used biodeposit output from oyster filtration to model chemical fluxes across the sediment-water interface (Testa et al., 2015; Testa et al., 2013). Essential model behavior is re-described here when necessary to convey key changes and model output, but details of previous iterations can be found in the aforementioned publications. Model development is divided into two parts: the formulations pertaining to oyster filtration and growth, collectively called bioenergetics, and adaptation of the biodeposit transport module to capture farm hydrology. For ease of understanding the way that the model captures these processes, we characterize three model modules and the methods for exchanging output among these below.

The primary model domain is a two-dimensional grid that models the advective-diffusive transport of particles with depth (z) across a single horizontal plane (x) of an oyster reef or farm. Particle removal from the water column was driven by oyster filtration in the bottom-most grid cells. In this latest iteration of ReefBioDES, an oyster bioenergetics model was coupled to the advection-diffusion model so that particle uptake drives oyster growth and biodeposit production. Collectively, the advection-diffusion and bioenergetic focused models are characterized as “Module 1” in Figure 2. Newly produced biodeposits are passed to a biodeposit resuspension and transport model (Module 2 in Figure 2) and undergo resuspension and possible export from the model domain or are immediately deposited and subject to partial degradation and delivery to a third module, SFM (Module 3 in Figure 2). The spatial-temporal modeling of biodeposit production and transport was facilitated by a sublayer state variable in Module 2 which retained those biodeposits that had not been degraded or exported for potential resuspension and/or degradation in subsequent time steps. Degraded biodeposits were averaged across the reef at every time step and summed over 24 hours to yield a daily rate of biodeposits produced per m^{-2}. Chemical transformations and exchanges between the water column and sediment (SFM) were modelled as a spatially implicit function of the daily rates of POM produced in Modules 1 and 2, and forced using local temperature, salinity, and dissolved oxygen data. Note that in the previous version of ReefBioDES, SFM was coupled to biodeposit production and transport and therefore spatially explicit.

Bioenergetics model development

Prior to the developments made here, ReefBioDES did not explicitly model ingestion beyond using the Ehrich and Harris (2015) maximum filtration rate formula and associated limitation factors to quantify food particle removal across an oyster reef. These equations were the result of a review comparing three models, each governed by oyster filtration, that were developed to a) model oyster growth using environmental parameters (Cerco & Noel, 2005), b) model phytoplankton removal using oyster size (Fulford et al., 2007) , or c) model oyster stocks using size classes (Powell et al., 1992). Analysis of these three models led to a weight-dependent maximum filtration rate (FR_i, $\mathrm{m}^3 \mathrm{oyster}^{-1} \mathrm{day}^{-1}$) that is qualified with environmental limitation factors including ambient temperature ($f(T)$), salinity ($f(S)$), and concentration of total suspended solids ($f(TSS)$):

$$FR_i = 0.17 * W^{0.75} * f(T) * f(S) * f(TSS) \quad (1)$$

where W is the individual oyster weight in grams dry weight (gDW) and the limiting factors are dimensionless (Ehrich & Harris, 2015).

Of the three limitation factors, temperature generally affects filtration the most. Ehrich and Harris (2015) adapted two Jordan (1987) derived formulas (Cerco & Noel, 2005; Fulford et al., 2007) to create a new $f(T)$. The function ranges from 0 to 1 and uses a reference temperature T = 27℃, where filtration is assumed to reach its maximum and declines thereafter. The effects of low salinity and high concentration of total suspended solids are modeled with piecewise functions:

$f(S)$ = 0 when $S < 5$; 0.0926 $* S - 0.139$ when $5 \leq S \leq 12$; when $S > 12$ (2)

and

$f(TSS)$ = 0.1 when TSS < 4 $\mathrm{g/m^3}$; 1.0 when 4 $\mathrm{g/m^3}$ < TSS < 25 $\mathrm{g/m^3}$; $10.364 *$ $\log(\mathrm{TSS})^{-2.0477}$ when TSS > 25 $\mathrm{g/m^3}$ (3)

All limitation factors range from 0 to 1 (Fulford et al., 2007). When coupled to the advection-diffusion transport equations, this filtration formula effectively simulates the oyster-driven reduction in water column particle concentration across the model domain.

The previous iteration of ReefBioDES used an empirical formula developed by Jordan (1987) which models biodeposition using a series of laboratory flume experiments—validated with field experiments—that measured *C. virginica* biodepositon rates. A multiple regression empirical model analysis of laboratory data resulted in a $\log_{10}$ biodeposition rate that is dependent on ambient temperature (T) and seston concentration (S)

$$\log_{10}\mathrm{biodep} = \beta_0 + \beta_1 T + \beta_2 T^3 - \beta_3 T^2 S + \beta_4 T^2 S^2 \quad (4)$$

where β_i are the parameter estimates yielding a rate of mg of biodepositon per gram dry weight oyster per hour mg gDW oyster^{-1} h^{-1} (Table 1). As temperature increases within the viable range for oysters, biodeposition also increases (Fig. 3).

Much work was invested into determining the appropriate modeling approach to incorporate a bioenergetics module within the existing framework of ReefBioDES. This work included a detailed review of 3 existing bioenergetics models, including a Dynamic Energy Budget (DEB) model (Lavaud et al., 2017) and a population dynamics model, ShellSIM (Hawkins et al., 2013). Formulations from a *C. virginica* bioenergetics model created by Cerco (2005) were ultimately chosen. This model was designed for use in a large-scale natural and restored reef model of oyster growth and population dynamics, which was combined with a module of water transport and biogeochemistry and an oyster benefits module. These bioenergetic equations were originally formulated to capture the influence of oyster physiology on C and N cycling, which required detailed consideration of energy partitioning within the oyster and the chemical composition of each energy store in terms of C, N, and P. Lastly, the Cerco (2015) model had a relatively high number of parameters that were estimated specifically for *C. virginica* whereas other models more commonly adapt parameters from studies on other bivalves.

Considerations of oyster physiology

The selection of formulas to quantify ingestion and biodeposit production was guided by oyster physiology. Although phytoplankton are the primary diet of *C. virginica*, oysters filter a range of organic and inorganic particles within a size range of 3-100 μm (Haven & Morales-Alamo, 1966). Their ability to efficiently ingest nutrient rich seston is due to several specialized organs which sort and transport mucous bound strings or slurries of particles. Non-mucous bound particles can also be internally transported through suspension. Lateral ciliary action on the gills generates an intake water current for filtration and respiration. The 4 layers of mucous-covered demibranches, two of which comprise a single gill, trap filtered particles based on size and chemical composition. A second set of independent, frontal cilia move these captured particles dorsally (towards the narrow, hinge joining two shell valves) to be transferred and further sorted by the labial palps—another soft, layered structure on the antero-dorsal side of the oyster. Mucous covered strings of particles are transported from the gills towards the labial palps via a marginal "food" groove that runs along the free edge of each demibranch. In contrast, particle slurries are transported via a ciliated basal tract that runs along the connection between each gill and the soma. Each gill demibranch corresponds to a labial palp, increasing efficient transport between the two (Ward et al., 1994). Suspended particles and those from the marginal food groove join those rejected from the labial palps, forming mucous coated spheres which are eventually sent to the mantle region to be ejected as pseudofeces.

All particle capture and transport up to the point before any mucous slurry enters the mouth is considered filtration. The process that follows is ingestion, where non-rejected material enters the mouth for processing by the digestive system. This distinction and terminology become important as equations to model oyster growth are described and assembled. The oyster digestive system consists of a mouth, short esophagus, stomach, crystalline style sac, digestive diverticula, midgut, rectum, and anus. Compact ribbons of feces are expelled through the cloacal cavity and are strong enough to maintain their ribbon structure as they are expelled into the environment (Galtsoff 1964). This detail is significant to model development because all biodeposits (feces and pseudofeces) are assumed to have the same structure and chemical composition, thus undergoing settling, transport, and degradation in the same manner. Biodeposits are also collectively sent to the sediment community for nitrogen transformations as a chemically homogenous mass. Thus, while feces and pseudofeces are not identical in structure nor composition, treating them as such is justified first by these similarities, and second by the fact that pseudofeces can make up a significant portion of biodeposition ((Foster-Smith, 1975; Tenore & Dunstan, 1973). A conversion factor of 4.8 mg N per gram of biodeposits (Jordan 1987) was used to convert biodeposits into a quantity of N for use by SFM.

Adaptation of bioenergetics model to ReefBioDES

The bioenergetics model chosen for implementation into ReefBioDES (Cerco, 2015) models pseudofeces as the excess of ingested material following filtration. Filtration refers to all material an oyster removes from the water column, which can either be rejected as pseudofeces or ingested through the alimentary systems. This conceptualization is appropriate because it distinguishes filtration from ingestion and enables feedback between the particles that enter the oyster and those that are removed from the water column. The key methods and equations of the Cerco and Noel (2015) *C. virginica* bioenergetics model are described here before their adaptation to ReefBioDES is detailed. The model uses joules as currency to maintain mass balance during internal energy transformations and exchanges with the environment. The governing equation for oyster weight becomes the difference between energy consumption (C) and energy expenditures in the forms of basal metabolism (BM), specific dynamic action (S), feces (F) and excretion (U):

$$\frac{dW}{dt} = \{C - [(BM + S) + (F + U)]\} \frac{1}{EPRD} \quad (5)$$

where EPRD (J gDW^{-1}) is the energy density of the oyster, a conversion factor used to translate between the energy content of food and oyster biomass. Consumption is modelled using a filtration formula similar to the Ehrich & Harris (2015) allometric formula used in ReefBioDES. Consumption, *actConE,* is simply the filtration rate multiplied by the energy contained in the water, known as *energyCon*, and is converted with a gDW multiplier to yield a rate in J s^{-1}. *EnergyCon* represents the potential energy available to an oyster in Joules per cubic meter of filtered water. Finally, consumption is given by

$$actConE = volRate * gDW * energyCon \quad (6)$$

where *volRate* is a filtration rate (m^3 gDW^{-1} d^{-1}). Ingestion (*fingest,* s^{-1}) is assumed to be some maximum fraction value that is a function of oyster weight:

$$fingest = fib \cdot DWtissue^{ing\_exp} \quad (7)$$

where *fib* is a base filtration rate and *ing_exp* is the exponent to relate oyster weight to ingested fraction. The ingestion fraction is multiplied by the energy density of an oyster (EPRD, J gDW^{-1}) to calculate the ingested portion. When consumption exceeds the maximum ingestion capacity, the remaining energy is released as pseudofeces, and the ingested portion continues to undergo energy transformations within the oyster. When ingestion exceeds consumption, all the consumed energy (*actConE*) goes to ingestion and no pseudofeces are produced.

Feces, excretion, and specific dynamic action are all constant fractions of consumption (0.5, 0.05, and 0.2 respectively). The remaining 25% of ingested energy is now “assimilated” energy. The final energy reduction before an oyster can accrue mass (i.e., grow) is the basal metabolic cost, described with the following two temperature and weight dependent formulas

$$respct = BM_{ro} * g(i)^{BM_{exp}} * e^{KTbmr*T(i)-Tr} \quad (8)$$

$$respireL = respct * g(i) * \frac{EPRD_g}{24} \quad (9)$$

If basal metabolism requires more energy than what was obtained through assimilation, the deficit is taken from the existing tissue biomass of the oyster. If the energy in assimilation exceeds the loss from basal metabolism, a condition index determines the fate of this remaining energy. If an oyster is below the condition index of 0.9 gDW, all energy is made available to tissue growth. Above this threshold, energy is first partitioned into shell using a fixed fraction ($F_s = 0.6$) and the remaining energy goes to oyster tissue. Note that reproduction is modelled in the original Cerco (2015) bioenergetics model, where if the oyster is > 6 months old the energy not used for shell building is divided evenly between reproductive material and tissue. Reproduction was not modelled in this study because the triploid oysters on an aquaculture farm would not require energy for reproduction.

Adaptation of ingestion formula to ReefBioDES

After considering the existing filtration formula of ReefBioDES and deciding on a bioenergetics model to adapt, this study chose to use a maximum ingestion rate to model oyster biodeposition. This method most closely resembles oyster physiology while also maintaining mass balance. Some of the reviewed models assumed ingestion was some fixed fraction of filtration and that pseudofeces is 1 – ingestion fraction. This formulation results in continuous pseudofeces production. If food availability is even mildly depressed, the fixed-fraction method would likely underestimate ingestion by not allowing a reduction in pseudofeces production so that the oyster can ingest more energy. A maximum ingestion rate avoids this issue by assuming that oysters will ingest food at some constant, maximum rate when environmental conditions allow. The maximum ingestion capacity of the oyster does not change. Instead, if the oyster is filtering below its maximum ingestion capacity rate due to food limitations, then all filtrate is ingested and no non-fecal biodeposits are produced. When filtration exceeds the maximum ingestion rate, all excess energy is released as pseudofeces. The bioenergetic formulations developed for this iteration of ReefBioDES used a hybrid approach between the existing filtration rate, fundamental concepts and equations from the Cerco (2015) approach, and experimental observations described in Cerco and Noel (2005).

Cerco and Noel (2005) review several studies which experimentally estimate oyster ingestion capacity using indirect measurements of pseudofeces production at different concentrations of suspended solids. The concentration at which pseudofeces begins is assumed to be the instant immediately after the ingestion capacity is reached. Using results from the Jordan (1987) experiments, where a seston concentration of < 4 mg L-1 resulted in very little pseudofeces production, Cerco and Noel (2005) determined a maximum ingestion rate in model units to be

$$\frac{4\text{ g seston}}{\text{m}^3} \cdot \frac{0.75\text{ organic}}{\text{total}} \cdot \frac{\text{g C}}{2.5\text{ g seston}} \cdot \frac{0.1\text{ m}^3}{\text{g C day}} = \frac{0.12\text{ g C ingested}}{\text{g oysterC day}}$$

Total suspended solids were found to be 75% organic (Newell & Jordan, 1983). Cerco and Noel (2005) apply a ratio of grams of carbon to grams of seston to convert into model units. The final conversion of 0.1 m^3 g C^{-1} d^{-1} is the filtration rate at TSS = 4 mg L^{-1} according to the function used to obtain *fTSS.* At the maximum ingestion rate, all food particles contained in filtrate are assumed to be ingested.

The Cerco (2015) concept of *energyCon*, which is the energy contained in a volume of filtered water, was used to model consumption. The first product of the bioenergetics model into the ReefBioDES environment was biodepositon (mass $oyster^{-1}$ $time^{-1}$), making the conversion to joules not immediately necessary. Consumption then became

$$\mathit{actConE\_TSS} = \mathit{energyCon} * Fr_i \quad (10)$$

and *energyCon* can remain in units of mg cm^{-3}. Similarly, ingestion I is

$$I = Fr_i * I_{max} \quad (11)$$

where Fr_i is the Erich and Harris (2015) filtration formula based on individual (i) weight, and I_{max} is the food particle concentration at which all filtered material is ingested (4 mg L^{-1}). For consistency with model units

$$\mathit{actConE\_TSS} = \mathit{energyCon} * Fr_i * * \mathrm{N}\left(\frac{\mathrm{oysters}}{\mathrm{m}^2}\right) \quad (12)$$

$$I = Fr_i\left(\frac{\mathrm{m}^3}{\mathrm{oyster}^{-1}\mathrm{day}^{-1}}\right) * \mathrm{N}\left(\frac{\mathrm{oysters}}{\mathrm{m}^2}\right) * \ I_{max}\left(\frac{\mathrm{mg}}{cm^3}\right) \quad (13)$$

From here, the conversion to joules is made using the energy density of the oyster (EPRD) and all calculations proceed in the previously described method of Cerco (2015). If consumption (*actConE_TSS*) exceeds ingestion (I) the difference between ingestion and consumption is pseudofeces. Biodeposition is the sum of pseudofeces and feces. Aside from the benefit of modeling oyster growth, a major product of these developments was to model oyster biodeposition in a way that maintain mass balance. The following section pertains to the fate of those biodeposits.

Hydrodynamic model overview

The hydrodynamic framework (Module 2) used in ReefBioDES (Kahover, 2022) to calculate the transport of suspended biodeposits depends on fundamental principles of mass conservation and remained the same in this new model iteration. Those equations are not reiterated here, but the formulas which characterize the roughness of a farm/reef are restated to explain how they were adapted.

The ReefBioDES model was originally formulated to simulate current velocities and boundary-layer effects around restored oyster reefs, where aggregations of individual oysters were modeled as individual and equally spaced roughness elements. To adapt this model to represent current flow through bottom cage aquaculture farms, roughness must represent an array of cages. The farm is made up of rows of evenly spaced cages where the rows are spaced further apart than the cages within them. Cages are modelled after those found at the CBL aquaculture site where observational data was obtained. The presence of cages is expected to reduce the depth-dependent velocity flow inside the farm relative to outside the farm. This attenuation is dependent on the density of cages. Cage density is characterized by the number of cages present on the farm, their size, and their relative distance to each other. Each cage was treated as a solid cuboid placed parallel to the sediment surface. Aquaculture cages have bars that allow water to flow through, but the assumption of a solid cube was justified by the fact that cages are substantially filled by between 4 and 6 bags full of oysters. Although the model was parameterized using the dimensions of an individual cage, their influence was considered on a farm-wide scale for model calculations of velocity attenuation and subsequent particle transport.

Current velocity flow, and its effect on particle transport, is influenced by the area of ground covered by cages relative to the total area of the farm. The advection diffusion subdomain is two-dimensional in the *x* and *z* directions, and all rates were standardized for a 1 m^2 section of farm in the y direction. Hydrodynamic conditions are similarly extracted into the third (*y*) dimension by assuming that cross stream conditions are homogeneous once defined (i.e., an infinite farm in the *y* direction). First, an initial grid of cages overlayed by the two-dimensional advection diffusion grid was created. This initial conceptualization of the farm was necessary to connect the two subdomains. The user inputs the desired number of cages in a single row of the farm (N_1), the length of each cage (*l*), and the approximate space between the edges of two cages. Because cages may not be equally spaced from each other, the user inputs two distances that represent the cage spacing in the *x* (s_x) and y (s_y) directions. A ‘functional unit’ of farm, for the purpose of linking filtration, biodeposition, and advection diffusion to the hydrodynamic calculations, was the distance from the left edge of one cage to the right edge of an adjacent cage. For cages of length 1 m and spacing s_x of 0.75 m, a functional unit is 1.75 m of farm length in the *x* direction. Total farm length was then calculated as the number of desired cages per row times the length of a functional unit (Fig. 4). This framework aided, but differed from, subsequent calculations of parameters that define the particle transport subdomain.

The initial grid of aquaculture cages provides a scaffold to calculate several key hydrodynamic parameters. The total farm area is made up of a grid of ‘reference units’ where a single cage exists inside a single reference area. Reference area is distinct from a functional unit because it is intended to capture the buffer area around a cage, or the extent to which a cage influences the current flow around it. The spacing between roughness elements for the purpose of hydrodynamic calculations is the geometric mean of the distances between the centers of adjacent cages, yielding

$$\lambda_{bio} = \sqrt{s_x * s_y} \quad (14)$$

Note that λ_{bio} is distinct from s, the spacing between cages used to partition oysters in the advection-diffusion model. The reference area, which includes the basal area of a cage, is then given by

$$F = \lambda_{bio}^2 \quad (15)$$

The total surface area of the farm, *S*, is the number of cages times the reference unit area (Fig. 5). This reference area is useful for determining potential biodeposit resuspension in the particle transport model, but all subsequent equations remain standardized to a 1 m farm width.

Estimating roughness length and boundary layer flow profiles

To describe the vertical distribution of mean current velocities near the boundary of the fluid region, logarithmic velocity profile, or *law of the wall* was applied. Experimental observations and numerical simulations of depth-dependent current velocities *u* as a function of distance *z* from the bed consistently shows a logarithmic relationship known as the mean-velocity profile. Under statically neutral, meaning there is no initial buoyancy or *vertical* acceleration of the water parcel and relatively flat conditions, the vertical profile of mean current velocity $u(z)$ can be approximated as

$$u(z) = \frac{u_*}{\kappa} ln\left(\frac{z-d}{z_0}\right) \quad (16)$$

where κ is the Von Karman constant (0.4), *z* is a reference height in the water column, and *d* is the displacement height from the apparent bottom. Friction or shear velocity u_* is associated with the shear stress at the bottom, a time dependent function defined as

$$\mathrm{u}_* = \overline{U}\left[\frac{1}{\kappa} ln\left(\frac{z_{ref}}{z_0}\right)\right]^{-1} \quad (17)$$

Here, $\overline{U}$ is the depth-averaged velocity at each model timestep, which is forced using upstream field-observations. z_{ref} is a chosen reference height in the water column. Finally, z_0 is the roughness parameter associated with the size and spatial distribution of specific roughness elements (e.g., oysters, cages, sediment particles). For specified z_0 and z_{ref} the model first calculates shear velocity, u_*, for each timestep (Eq. 16) and then current velocity $u(z)$ is calculated for each vertical grid cell at height z (Eq. 15).

Much attention has been given to the calculation of roughness length both generally in fluid dynamics and specifically in the development of ReefBioDES. In ReefBioDES, different calculations for roughness parameters are used for different purposes. The equations described here were implemented into the previous iteration of ReefBioDES after a comprehensive review of several potential equations to capture the biogenic roughness caused by oysters (Kahover, 2022). Roughness parameter z_0 was exclusively used in equations to characterize average across farm and reef velocity attenuation. z_0 was first defined by Forsyth (2014) when developing the particle transport model that serves as the foundation for ReefBioDES. In the method of Butman et al., (1994)

$$z_0 = \frac{\eta_0}{30} \quad (18)$$

where η_0 is oyster shell height measured perpendicularly from the sediment bed. This same formulation was used in Kahover (2022). However, when applied to roughness based on cage height rather oyster height, this approach resulted in serious model instabilities. A sensitivity analysis of z_0 revealed that a) there was a narrow range of stable z_0 values ($0.003 < z_0 < 0.02$), and b) model results showed little variation within this range with the exception of the two most extreme values. Model simulations proceeded with an intermediate, stable value of $z_0 = 0.0052$ for all present farm simulations, recognizing that this problem must be addressed and solved in future work.

Another roughness parameter, z_{0bio}, was incorporated into the previous iteration of ReefBioDES. This value was used to calculate the magnitude of shear stress experienced by the sediment surface for the exclusive purpose of determining potential resuspension and transport. z_{0bio} depends on the frontal area index parameter λ defined as

$$\lambda = \frac{Nbh}{S} \quad (19)$$

where N is the number of roughness elements and b and h are the average width and height, respectively, of the roughness elements (Fig. 6). In this case, the frontal area index can be simplified using the reference area to become

$$\lambda = \frac{bh}{F} \quad (20)$$

which essentially characterizes the ratio of surface area of the normal facing side of a roughness element to the density of roughness elements (i.e., cages). Recall that F is dependent on the distance between the centers of roughness elements, meaning that lambda is inversely related to cage density. The original formulations developed and tested by Kahover (2022) were deemed appropriate for use in modeling the roughness introduced by aquaculture cages for this purpose. For $\lambda < 0.1$, Lettau (1969) gives

$$z_{0bio} = 0.5 * h * \lambda \quad (21)$$

In the method of Theurer (1973), for $0.1 < \lambda < 0.25$,

$$z_{0bio} = h(1.6\lambda * (1 - 1.67 * \eta) \quad (22)$$

where $\eta = {}^{Nbl}/_{A}$ is the skin area index.

Finally, for $\lambda > 0.25$, Styles (2015) gives

$$z_{0bio} = \frac{5h}{30} \quad (23)$$

In the cages case h is cage height, but it is replaced by η_0 for reef simulations. Cage dimensions (h = 0.75 m, l = 1 m, and b = 1 m) and spacing (s_x = 0.75 m and s_y = 1 m) were kept constant in farm simulations, yielding $\lambda = 0.214$ (Eq. 23) and $z_{0bio} = 0.179$ (Eq. 25).

There are three distinct flow regimes that model, generally, how currents can flow over multiple roughness elements. The first is an isolated flow, where a roughness element is sufficiently distanced from other elements so that flow around the elements is unaffected by the flow around other roughness elements. Considering this first scenario, where each cage behaves independently as a single, isolated roughness element, the cage exerts a force on the surrounding water as the current is forced over and around it. The subsequent gradient of lower pressure along the top of the cage and higher pressure directly upstream and downstream results in increased current velocity above the cage and decreased current velocity directly in front of and behind the cage, which generates increased turbulence downstream.

A second flow regime is produced when at a certain density of cages their proximity creates a state where the interactions of current flowing around each cage become important in the calculations of drag. Raupach (1992) introduced the concept of effective sheltering area (*A*) and volume (*V*) to describe the interactions of multiple roughness elements on current flow (Fig. 7)

$$A = c\frac{\lambda \cdot S}{N} \cdot \frac{\bar{U}}{u_*} \quad (24)$$

$$V = A \cdot h \quad (25)$$

Here c is an empirical constant (~ 0.4). A depends on shear velocity u_* (Eq. 20) and the depth averaged velocity $\bar{U}$ for a given timestep. The definitions of A and V are simplified using λ. The λ formulation proposed by Raupach (1992) is only valid for $\lambda \leq 0.1$, which occurs when there are few roughness elements and/or the elements are sufficiently small. At a low-density of roughness elements (i.e., there is significant space between individual elements), or in the case where elements are sufficiently small, it is reasonable to assume that the entire frontal facing area senses the impact of the normal flowing current. As more roughness elements occupy the same surface area, current facing roughness elements begin to block downstream elements. For λ to be less than 0.1 at the farm sites where forcing and validation data were collected, the density of cages would need to be approximately 1 cage per 7.5 m^2 given the dimensions of the cages. The actual cage density of the study site was closer to 1 cage per 3.5 m^2.

The third flow regime describes a critical point at which multiple roughness elements become close enough together that they behave as a single, large roughness element. The Raupach (1992) calculation for frontal area index does not entirely account for the two flow behaviors where roughness elements interact. Because this theory is used to represent multiple cages which are relatively large, an adjustment to lambda was made to accommodate $\lambda > 0.1$ which is detailed in the following section.

To model the influence of additional roughness elements (i.e., cages) on current velocity, we estimated the total drag force across the farm for a given density of roughness elements. The method of Shao and Yang (2005) was used to calculate the total farm drag. This same method was used in the previous iteration of this model (Kahover, 2022). Shao and Yang (2005) derived their summation of total drag on a rough surface from the Raupach drag partitioning theory (1992). Raupach represented total drag (τ_T) as the sum of the pressure drag (τ_f) acting on the roughness elements and skin drag (τ_s) from friction along the surrounding bottom. Yielding

$$\tau_T = \tau_f + \tau_s \quad (26)$$

Recognizing the limitations of λ at high densities of roughness elements, Shao and Yang (2005) proposed the following modification for the calculation of effective frontal area index, Λ_e

$$\Lambda_e = \frac{\lambda}{(1-\varphi)^n} * exp\left(-\frac{a\lambda}{(1-\varphi)^n}\right) \quad (27)$$

where *n* and *a* are estimated constants assigned values of 6 and 0.1, respectively. Shao and Yang (2005) propose an additional drag force τ_{re} that represents the skin drag exerted on the roughness elements. The new partitioning scheme for τ_T becomes

$$\tau_T = \tau_f + \tau_s + \tau_{re} \quad (28)$$

where, as before, τ_f is the form drag and τ_s is the sediment skin friction. Model calculations proceeded with the Shao and Yang (2005) method for drag partitioning and effective frontal area.

When calculating the frequency of biodeposit resuspension, only sediment skin drag was considered. Form drag τ_f and the skin drag associated with the cages τ_{re} were both ignored. Calculations of sediment skin drag consider the interstitial bed space between cages and yield overall farm current velocities. The method of Shao and Yang (2005), adapted from Raupach (1992), is used to calculate the drag partition. The ratio between skin drag τ_s and total drag τ_T is defined using effective frontal area Λ_e as

$$\frac{\tau_s}{\tau_T} = \left(1 - \frac{\beta_c \Lambda_e}{1+\beta_c \Lambda_e}\right) exp(-b_s \eta) \quad (29)$$

Here, $\beta_c = C_R/C_s$ is the ratio of the drag coefficient for a single roughness element (C_R) to the drag coefficient of the surrounding sediment (C_s). In the method of Shao and Yang (2005), a value of $b_s = 5$ was chosen so that for small λ values, the modified ratio of τ_s / τ aligns with the original Raupach (1992) ratio. C_R was approximated to be 0.3 (Denny, 1988).The calculation of C_s is given by

$$C_S = \left(\frac{u_{*grain}}{\bar{U}}\right)^2 \quad (30)$$

Here, u_{*grain} is the sediment friction velocity and $\overline{U}$ is the depth-averaged velocity for a given timestep. Sediment friction velocity is calculated using a chosen reference height, ref_h, and depth averaged velocity $\overline{U}$ at a given timestep,

$$u_{*grain} = \frac{2}{5}\overline{U}\, ln\left(\frac{ref_h}{z_{0grain}}\right)^{-1} \quad (31)$$

where z_{0grain} is the roughness length associated with the biodeposits in the sediment, akin to the biogenic roughness length $z_{0\text{bio}}$. Finally, to solve for τ_s, total shear stress τ_T at each timestep was expressed as

$$\tau_T = \rho u_*^2 \quad (32)$$

where ρ is the density forced with environmental data and u_*. Substituting τ_T into equation 28 and isolate skin drag of the sediment bottom (τ_s).

In the absence of additional roughness elements, total bed shear stress τ_T is equal to the skin drag of the sediment bottom τ_s. Substituting τ_s into equation 31 yields

$$\tau_s = \rho u_{*\text{grain}}^2 \quad (33)$$

where u_{*grain} is the sediment friction velocity (Eq. 20), modified as

$$u_{*grain} = \frac{2}{5}\overline{U}\, ln\left(\frac{ref_h}{sed_{z0}}\right)^{-1} \quad (34)$$

Here, sediment roughness length $sed_{z0} = 0.002$ is used in the calculation of friction velocity. The occurrence of particle suspension/resuspension depends on the calculated value for shear stress (τ_s) and a chosen critical shear stress (τ_{crit}) value of 0.05 Pa (Holyoke, 2008). Resuspension and particle transport is determined for each hourly model timestep on a reef-wide scale. When there is no particle resuspension ($\tau_s < \tau_{crit}$), all newly produced biodeposits are sent to an intermediate sublayer which contains non-decayed biodeposits from previous timesteps.

The quantity of biodeposits that was considered settled at each timestep was calculated as the biodeposits produced by the oysters less the amount of biodeposits which exited the reef or farm domain during suspension and/or resuspension. Two final transformations occurred before biodeposits from Module 2 were delivered to SFM (Module 3). First, a decay function modelled with an exponential constant of -0.064 simulated the decay of biodeposit from their ribbon-like structure. The non-decayed portion of biodeposits remained in the biodeposit sublayer for future resuspension and eventual decay. Second, a dilution factor was introduced to simulate the possible settling of biodeposits on surfaces other than the bottom (i.e., oysters) and was calculated as the inverse of the total surface area of the oysters contained in a square meter section of farm. As such, the dilution factor increased with oyster density. The amount of particulate organic nitrogen (PON), carbon (POC), and phosphorus (POP) contained in a mass of biodeposits were constant values (4.8, 34.8, and 0.58 mg g^{-1} biodeposits) derived from regional data.

Simulations

To test general model performance after incorporating aquaculture cages into the spatial domain and adding the bioenergetics model, initial simulations were run with hourly-averaged data from a two-week observation period, including forcing functions of chlorophyll-a, total suspended solids, current velocity, and temperature. These simulations were validated with data from the same period collected at the mid-farm station. To answer the primary research questions of this study, five model simulations were forced with 5 months (April to August 2020) of data obtained from a YSI EXO2 sonde measuring temperature, salinity, and chlorophyll-a at a long-term monitoring station near the aquaculture lease (CBL, Pier, 38.317 deg N, -76.450 deg W). Initial oyster weight was set to 1gDW, cage dimensions were set to 1m in width and length and 0.75m in height (based on cage measurements taken at the aquaculture lease where these data were obtained), and row and column spacing were 0.75m and 1.0m, respectively. All simulations (Table 2) included the full potential of ReefBioDES, including the bioenergetics module.

Sustainable and profitable aquaculture practices depend on maximizing oyster growth, which is limited by food availability. Model formulations and previous simulations demonstrate that oyster density and farm length significantly influence particle availability across a reef, or in this case a farm. Additionally, deleterious effects of oyster farming may be more likely to occur in operations with large footprints and/or high oyster densities. Therefore, to assess model behavior at different oyster densities, a “high-density” simulation of 800 oysters per cage and a “low-density” simulation of 200 oysters per cage were run, both at a farm length of 50 m. Two additional simulations were run of varying reef lengths, a 35 m “small farm” and a 70 m “large farm”, with a constant density of 300 oysters per cage. In all of these, the original Jordan (1987) formulation for biodeposition was modelled in tandem to compare the results of biodeposition calculated with the new bioenergetics module.

Modeled nutrient dynamics on the farm are influenced by more than the rate and quantity of biodeposit production. The distribution of biodeposits, frequency of resuspension (which varies with the density of roughness elements), and farm size will all influence potential transformations of nitrogen. The four chosen farm simulations of varying farm lengths and oyster densities gave insight into the combination of factors that influence nitrogen cycling. To obtain reference values of key chemical processes on bare sediment, the sediment-water chemical flux model was forced with the same outside platform farm data used in the oyster simulations, but run without additional POC, PON, and POP from oyster biodeposition. This simulation, called the no-oyster scenario, provided a baseline to measure the relative impact of oyster aquaculture and restored reefs on local nutrient dynamics under the same environmental conditions.

Finally, a reef simulation was run with bioenergetics to simulate the growth and local environmental impact of oysters that were evenly distributed across the model domain, and whose biodeposits were more likely to undergo resuspension due to the decrease roughness associated with oysters compared to cages. Density and spatial domain for the reef simulation were chosen to match the length of the large farm simulation (70 m) and the overall farm density of both the large and small farms (~170 oysters m^{-2}).

Results

Model validation and interpretation of observations

Two-week model simulations were run to capture two time periods, including spring (April 2021) and summer (July 2021). Field observations collected at the leading edge of the farm served as forcing data and included temperature, salinity, chlorophyll-a (CHLA), dissolved oxygen (DO), and current velocity. Modelled temporal and spatial patterns of CHLA and total suspended solids (TSS) concentrations and current velocity were compared against both high-frequency (15 minute) current velocity and CHLA data collected at the mid-farm station (monitoring station in the middle of the oyster cage array, Fig. 1) and discrete water-column CHLA and TSS observations made during a summer tidal survey. The tidal survey spanned the transect that mapped a gradient from outside the cage array through the cage array (Fig. 1). For discrete samples, both surface and bottom water samples were collected at four stages of a tidal cycle at each of the eight stations. Biodeposition rates were also compared to measured sediment trap collections at the locations pictured in Figure 1.

Model-observation comparisons revealed that simulated across-farm patterns were similar to field observations, but changes in CHLA within the model differed in magnitude from the observations. For example, CHLA concentrations extracted from the middle of a two-week simulation showed a similar pattern as the mid-farm validation data, but modelled CHLA was typically 6 μg L^{-1} lower than observations (Fig. 8). Model simulations produced an obvious chlorophyll gradient across the farm, where oyster filtration resulted in downstream chlorophyll depletion of 4 μg L^{-1} near the bottom and 2 μg L^{-1} near the surface (Fig. 9). These depletion rates were also evident in the discrete measurements of CHLA but were tide-stage-specific. For example, three of the four tidal cycle surveys showed evidence of within farm CHLA depletion (Fig. 10). During low tide, bottom water samples, and to a lesser extent surface samples, showed a clear reduction in total CHLA at sites within the farm footprint. During low tide, note that the oyster cages were comparable in height to the water depth. At flood tide, surface and bottom water CHLA concentrations decreased in the downstream direction (station 5 to station 1). In contrast, ebb tide bottom waters had higher CHLA values within farm, peaking at mid-farm station 3.

Discrete and high-frequency (15 minute) TSS concentrations were also analyzed as proxies for the impact of modeled oyster activity and for comparison to CHLA distributions over the tidal cycle. Like CHLA, surface TSS samples measured via both sampling methods showed a modest (~2-6 mg L^{-1}) reduction in concentration during flood and high tides, and ebb tide TSS was also reduced within the farm. In contrast, low tides showed the opposite or no trend (Fig. 11). TSS and turbidity were often higher in bottom samples within the farm, especially during ebb and low tides. Although TSS is not explicitly modelled but rather estimated from CHLA, these observations suggest a lack of correlation between TSS and CHLA in bottom waters, which likely reflects difference in the relative effects of filtration and resuspension on these variables. In-farm turbidity was reduced during low and high tides and decreased in the downstream direction from the mid-farm station at flood tide (Fig. 12).

Current velocity measurements taken at a bottom platform deployed in the middle of the aquaculture farm (mid-farm site; Fig. 1) were compared with model predictions of velocity at the surface and bottom (Fig. 13). The observed mid-farm velocity was depth averaged (in the same manner as the model forcing data from the upper farm platform) and comparisons were made over the 2-weeks of available validation data and simulations results. In general, modelled bottom velocities were 2-3 times lower than what was measured at the mid-farm platform (Fig. 13). The absolute differences between modeled surface and bottom velocity (and between the model and observation) were much smaller at slack tide and amplified during max flood or ebb tide. Because the modelled vertical velocity profile is idealized as being uniform across the reef (*x* dimension), the observed, depth-averaged velocity is expected to fall in between the surface and bottom predictions. Modeled velocity estimates the average effect of the farm, while the measured velocity on the mid-farm platform reflects an area of farm that would be expected to have higher local bottom velocities. These results were similar across both seasons and provide a basic validation of the model implementation.

Simulated biodeposition rates were compared against sediment trap data collected during both the spring and summer periods. Sediment traps were deployed for approximately 24 hours at stations 1, 2, 3, 4, 5, and 6 in the spring and summer (Fig. 1). Observed deposition rates were higher in the summer than spring at all stations except the shoreward station 6 (e.g., between the farm and the shoreline) (Fig. 14). There was generally an inverse relationship between deposition rates and organic composition. This relationship was most notable at mid-farm station 3, with a peak summer deposition rate of 51.52 g m^2 h^{-1}, of which 5.02 percent was organic, compared to a spring deposition rate of 7.84 g m^2 h^{-1}, of which 13.57 percent was organic. In-farm summer deposition rates were, on average, higher than outside the farm; however, station 2 was only slightly higher than station 1 (14.75 and 14.34 g m^2 h^{-1}, respectively) and both stations were lower than the shoreward station (17.25 g m^2 h^{-1}) in both seasons. Measured organic deposition rates, when compared to model estimates of biodeposit production within a simulated farm, suggest that a significant portion of biodeposits settled out of the water column (Fig. 15). If the mean model biodeposit production rate of the 2-week summer simulation is a reasonable approximation, it would suggest that about 80% of the mid-farm biodeposits produced would settle based on station 3 data, and that half of the biodeposits would settle based on the other in-farm stations 2 and 4. Although sediment trap data suggests that deposition rates within the farm footprint are, on average, higher than outside of the farm, the comparable values at stations 1 (outside farm), stations 2 and 4 (inside farm), and station 6 (inshore of farm) may reveal that advective flows and wave-induced resuspension led to biodeposit export from the site (Testa et al. 2015). Biodeposition rates calculated using the Jordan (1987) formula as a comparison were higher than those in model simulations, and therefore significantly higher compared to observed organic depositions rates using sediment trap data. The alignment between the modelled biodeposit production and observed deposition may suggest that the new bioenergetics approach (Module 2) in this study was more appropriate for simulating farm conditions at this location.

Results from long-term simulations: Patterns of CHLA removal and oyster growth

Oyster density and farm length controlled the degree of downstream CHLA depletion resulting from oyster filtration in cages, an observation consistent with previous iterations of this model as applied to oyster reefs (Forsyth, 2015; Kahover, 2022). Average CHLA depletion was calculated as the depth integrated, absolute difference between CHLA concentration in the first and last cells , summed across timesteps and divided by the time of the simulation. The small and low-density farm both had similar concentration differences, 25.51 and 25.80 μg L^{-1}, respectively. In contrast, the high-density farm had an oyster density 4 times that of the low-density farm and an average concentration difference of 58.01 μg L^{-1}, just over 2 times greater than the low-density farm (Fig. 17). The high-density farm and reef had similar concentration differences ~58.01 μg L^{-1}. For all simulations, the degree of upstream to downstream depletion of CHLA increased over time as water temperature and filtration rates increased into the summer growing season (data not shown). In some simulations, this depletion resulted in food limitation that influenced oyster growth rates.

Because oyster growth is dependent on food availability, oyster growth was also inversely related to oyster density and farm length in all model simulations, as more oysters consume and demand more food and forcings of chlorophyll remained the same throughout all simulations. The average growth rate of an individual oyster in each model simulation was calculated by subtracting the initial tissue weight (set to 1gDW for all simulations) from the final tissue weight at the end of a simulation. For a given simulation, each cell that was part of a cage had the same number of oysters (5-7 oysters per cell depending on the simulation) and growth was tracked independently for each cell using the bioenergetics calculations. The high-density farm had the lowest average growth rate, less than half of all other farm scenarios, while the low-density farm had the highest growth rates (Fig. 17). A closer look at the spatial variation of oyster growth revealed two patterns: oyster growth declined the further an oyster was from (a) the leading edge of an individual cage and (b) the leading edge of the entire farm (Fig. 18). Furthermore, analysis of the average growth rate across a subsection of each farm showed that average growth rates on the high-density farm became negative at a mid-farm point of approximately 35 meters into the farm (Fig. 18). The small farm scenario is excluded from this figure because it was only 35 m in length.

The long-term effect of a reduced growth rate with distance from the leading edge of the farm was evident in the spatial variation of final oyster shell length. Shell biomass was explicitly modeled as part of the bioenergetic formulations; however, shell length was not. The final tissue gDW of an oyster was converted to shell length using an empirical formula derived from regional data of triploid oysters ($\text{gDW} = 0.00005*(\text{mm shell length})^{2.39}$; see Oyster BMP Expert Panel review 2016). Figure 19 shows the final shell lengths of each oyster in the first 9 cages, or reef equivalent, of the farm, where each bottom cell that contained oysters is represented. Overall, oysters became smaller with distance from the farm's leading edge, and this trend was more obvious in the high-density scenario. A similar pattern of decreasing shell length emerged inside of each cage; however, there were large differences between the minimum and maximum shell length inside a cage that were not observed across the entire farm. This pattern is most obvious on the high-density farm, where the magnitude of oscillating shell lengths across the horizontal space representing a cage is much greater than all other simulations.

Comparing bioenergetic output between the large farm, small farm, and reef simulations, which all had the same oyster density, demonstrated that the spatial arrangement of oysters (i.e., cages versus reefs) had a significant impact on oyster physiology. For example, the large farm was twice the length of the small farm, and food limitation on the larger farm resulted in a lower average growth rate (2.39 and 2.20 mgDW d^{-1} for the small and large farms, respectively). The simulated reef was also twice the length of the small farm, yet the average growth rate was much lower (1.58 mgDW d^{-1}) than either the small or large farm simulations. This pattern was explained by the spatial patterns of oyster growth that emerged across the model domain. Because each cage was modeled as several smaller, consecutive cells containing oysters, oyster growth rates varied significantly within a given cage (Fig. 18). Despite the relatively large differences between the highest and lowest growth rates inside a cage, the large farm still had an average growth rate that was higher than the reef (1.58 mg d^{-1}) (Table 3).

Results of long-term simulations: Biodeposition rates and nutrient cycling

Biodeposition rates in model simulations were estimated from the pseudofeces and feces produced by the bioenergetics model, which allowed for a comparison of food-limitation, oyster density, and farm size effects on biodeposition rates. For the purposes of this analysis, it was convenient to report biodeposit production as grams of N, using the same conversion factor of 4.8 mg N per g biodeposits (Jordan, 1987) that is used in ReefBioDES. Farm size was positively correlated with biodeposit production, an observation that is consistent with findings in the previous iteration of ReefBioDES, as applied to reef scenarios (Kahover, 2022). However, the relationship between density and biodeposit production, which had been well established to be positive in previous iterations, was non-linear. For example, total biodeposit production from the high-density farm (~245 kg N) was only slightly larger than the reef scenario (~213 kg N), yet the large farm contained two times more oyster biomass and had an o yster density almost 2.5 times higher than the large farm and reef (Table 4). This relationship revealed the close association of oyster physiology and biodeposition. When oysters experienced food limitation, most or all filtrate was sent to the digestive system and little to no pseudofeces were produced. Because pseudofeces are a major component of biodeposition, rates of organic matter deposition were lower than might be predicted in the high-density scenarios. The constraint of food limitation on biodeposit production is clearly illustrated by comparing the bioenergetics model-based rates to the non-food limited rates predicted from Jordan (1987), used in previous versions of ReefBioDES (Kahover 2022; Fig. 20). The bioenergetics-based biodeposit production estimates were ~68-80% lower than those computed from Jordan (1987). The total biodeposit production did not vary noticeably between the large farm and reef (Fig. 20), but there were distinct spatial patterns in the farm relative to the more uniform reef simulation (Fig.21). Biodeposition was also highest on the leading edge of the cage. The relative magnitude of biodeposition rates did not change among scenarios during the time-course of the simulation (Fig. 22), and biodepositon increased as the summer growing season progressed. Apart from the first 6 weeks, the Jordan (1987) biodeposition formula estimated higher rates of biodepositon than the bioenergetics module did. This was true for all simulations, including the reef.

The delivery of biodeposits to SFM was moderated by resuspension and transport off the model domain. Resuspension occurred during 55 and 76% of time steps in the farm simulations and reef simulation, respectively. Resuspension occurred at the same timesteps in all farm simulations because the array of cages and set of forcing velocities were constant. Figure 23 shows the percent of biodeposits exported from a given farm during each time step where resuspension and transport occurred. The fraction of biodeposits exported from the small farm at a given timestep was generally higher than the other simulations, but because biodeposit production was relatively low on the small farm, the total mass exported remained low. Although resuspension occurred more frequently on the reef, the relative percent of biodeposits exported during each timestep was generally lower than the farm simulations (Fig. 24). It is worth noting that resuspension is modelled with tidal current forcing velocities, excluding wave action.

The relationship between food availability, growth, and biodeposition ultimately determined the biogeochemical transformations and exchanges simulated in the underlying sediments. Key outputs from the sediment flux/biogeochemical model (SFM), including ammonium (NH_4^+) and nitrate (NO_3^-) fluxes, denitrification, and ammonium recycling efficiencies and denitrification efficiencies, were analyzed for temporal patterns. Where appropriate, rates were summed over the duration of a simulation to compare the magnitude of N transformations in a simulation over time. For example, ammonium production rates were elevated in all simulations with oysters (i.e., relative to “no oyster scenario”; Fig. 25). The small, large, and low-density farms all had comparable rates of ammonium flux (Fig. 25), which is consistent with their comparable rates of biodeposition (Fig. 22). Ammonium fluxes on the low-density and small farm simulations were nearly identical. Ammonium fluxes were also highest in the reef and high-density simulations, reaching peak rates of 1000 μmol m^{-2} d^{-1}. In all simulations with oysters, ammonium production peaked during mid-summer before dropping off again as temperatures fell towards the end of the simulated period (April–August 2020).

For the first 2 months of the simulation (April and May 2020), nitrate flux for all simulations remained relatively high (around 20 μmol m^{-2} h^{-1}) and was positive, where fluxes were directed out of the sediments (Fig. 25). As oyster biodeposit production increased in response to warming temperatures, nitrate flux was reduced for all simulations and was directed into the sediments for the reef and high-density simulations. The low-density and small and large farms had similar temporal nitrate flux patterns that were distinctly different from the reef and high-density farms, where the small, large, and low-density farms had nitrate fluxes that oscillated around zero but were not directed consistently in or out of the sediments (Fig 25). Nitrate fluxes in the reef and high-density farm were typically between 10 and 30 µmol m-^{2} h^{-1} lower. Peaks in deposition rates correlated with negative nitrate flux values. In week 14, for example, a spike in biodeposition across all simulations induced negative nitrate flux values ranging from -12.71 µmol m-^{2} h^{-1} in the low-density scenario to -40.98 and -42.00 µmol m^{-2} h^{-1} in the reef and high-density simulations, respectively. These were the lowest simulated values for all reef/farm configurations, indicating an inverse relationship between biodeposition and nitrate flux. In contrast, the no-oyster simulation showed relatively stable nitrate flux values, slightly negative in the last half of the simulation (Fig 25). For comparison, the modeled nitrate fluxes were extremely small relative to the ammonium fluxes.

All simulations containing oysters demonstrated enhanced rates of denitrification compared to the no-oyster reference simulation, but with varying magnitudes and not at all timesteps (Fig. 26). In the first 2 weeks, the no-oyster scenario, which is interpreted here as representative of bare-sediment, had lower rates of denitrification than the other scenarios, but all fluxes were relatively low. The same seasonal peak in biodeposition that reduced nitrate flux also reduced denitrification rates in all scenarios with oysters. Unlike the ammonium and nitrate fluxes, denitrification rates were highest in the large farm and low-density scenarios, revealing non-linear relationships between denitrification and biodeposition. For example, an inverse relationship between biodeposition and denitrification developed around June for all simulations and was apparent for the remainder of the simulation duration. N removal via denitrification was relatively low on the small (150.40 g N) and high-density (~180 g N) farms, and higher on the large and low-density farms (Fig. 26). Differences between simulated denitrification rates and N removal are because the latter process depends on the space over which these rates are observed (i.e., farm size; Table 4). Consequently, while the reef simulation may have had the lowest rate of denitrification per square meter over the time-series, the N removed via this process was the second highest of any simulation (251.71 g N) because oysters occupied a much higher fraction of the farm. Finally, the large farm represented an intermediate scenario where denitrification rates generally fell halfway between the other scenarios, but the relatively large farm surface area resulted in the highest calculated N removal via denitrification (282.40 g N; Table 4). These observations led to two important findings: a) both oyster density and farm size controlled denitrification rates on simulated oyster farms (and reef), and b) the spatial configuration of oysters (i.e., farm versus reef) influenced denitrification potential when density and size are controlled. The first finding is consistent with simulation results from the last iteration of ReefBioDES (Kahover, 2022), and this study expands those findings to include aquaculture farms. The second finding provides insight into how N cycling on oyster aquaculture farms may differ from restored or natural reefs, which was the second research question this modeling exercise set out to inform.

A common feature of farm and reef simulations was a high rate of ammonium flux relative to the other N fluxes. Ammonium fluxes increased with warming temperatures, reaching peak values >1000 μmol m-^{2} h^{-1} in in the high-density and reef simulations, and peak values ~600 and ~500 μmol m-^{2} h^{-1} on the large farm and the small/low-density farms, respectively. In contrast, the no-oyster scenario showed almost no ammonium flux for the duration of the simulation. As water temperatures cooled towards the end of the summer, ammonium fluxes also decreased but were elevated compared to the first several weeks of the simulations. For all oyster simulations, ammonium recycling efficiency (%), formulated by the equation

$$\text{Ammonium Recycling Efficiency (\%)} = \frac{\mathrm{NH_4}}{\mathrm{NH_4^+ + NO_3 + N_2 - N}} \times 100$$

was calculated to examine the balance between N removal and N regeneration processes in the scenarios. For all scenarios, ammonium recycling efficiency reached 80% within the first 3 months (Fig. 27).

Similarly, denitrification efficiency, expressed as

$$\text{Denitrification Efficiency (\%)} = \frac{\mathrm{N_2 - N}}{\mathrm{NH_4^+ + NO_3 + N_2 - N}} \times 100$$

was calculated for each simulation. Compared to the no-oyster scenario, denitrification efficiencies in all simulations declined dramatically within the first 2 months, much earlier than rates of ammonium and nitrate flux or denitrification began diverging from the no-oyster scenario (Fig 27). Similarly, differences across simulations emerged earlier for denitrification recycling efficiencies compared to other modelled N processes. Both results are explained by a decrease in the aerobic layer depth (data not shown) following influx organic matter (i.e., biodeposits), where nitrification (an aerobic process) was limited by sediment oxygen availability and denitrification became nitrate limited.

Explicitly modeling biomass accretion in oyster tissue and shell made it possible to quantify N removal via assimilation and compare these values to modelled denitrification and burial. Only biomass that accumulated during the simulation was used to calculate tissue and shell N removal so as to capture only the processes (i.e., growth) that occurred simultaneously with indirect N removal, effectively making direct N removal a function of growth and farm/reef biomass. For all simulations, the dominant mechanism of N removal was either via tissue sequestration or denitrification. N removal via burial ranged from 59.40 g N on the small farm to 130.04 g N on the reef, which was approximately 40 to 55% of the N removed via denitrification, a substantial percent. At the small, large, and high-density farms, more N removal occurred via tissue sequestration than denitrification and the opposite was true for the low-density farm and the reef (Fig. 28). All forms of N removal except burial were higher on the large farm compared to the reef, despite having similar site characteristics (oyster density ~170 oysters per m^2 and reef/farm length = 70 m). The large farm appears to represent a combination of farm length (70 m) and oyster density (172 oysters per m^2) where N removal via tissue and denitrification are both maximized. It is important to note that if the total harvestable biomass of oysters on a farm/reef is used instead of the biomass accumulated during the 5 months of simulated growth, N removal via tissue and shell would be highest on the high-density farm, which had a harvest biomass 1.7 times that of the large farm.

Discussion

The sections below discuss results of the long-term model simulations and provide an overview of impacts of bottom cage aquaculture on water quality and food availability, bioenergetics, and nitrogen cycling. A final section outlines suggestions for future work and considerations regarding model assumptions.

Assessment of coupled bioenergetics model

Wide-spread food limitation was not expected to occur based on the environmental conditions of the spring and summer forcing data; however, the patterns of simulated oyster growth, especially in the high-density farm simulation, clearly quantified that limitation did occur. Validation results suggest that simulated chlorophyll depletion was overestimated, where modelled concentrations were ~42% lower than field observations. The across farm chlorophyll distribution showed cycles of depletion across a cage and then replenishment of food where the next cage began. This oscillatory pattern explains why downstream oyster growth continually slowed as summer progressed—their growth was limited by the compounding influence of large scale, across-farm chlorophyll depletion *and* within cage depletion by upstream filtration.

Chlorophyll depletion within the farm influences oyster biodeposit production and deposition rates. As oysters experienced food limitation, most or all filtrate was sent to the digestive system and little to no pseudofeces were produced. Because pseudofeces is a major component of biodeposition, rates of organic matter deposition decreased; however, where oyster density and/or biomass was large enough, biodeposit production across the farm remained high, even if individual filtration rates were reduced. In the case where biodeposit production was limited by food availability, organic matter deposition would have decreased. In this iteration of ReefBioDES, increased biodeposit production was associated with lower rates of denitrification, but this relationship was influenced by biodeposit resuspension and export from the model domain.

High stocking densities on oyster farms have been shown to be inversely related to oyster growth and condition index (Capelle et al., 2020), and this iteration of ReefBioDES appears to capture that relationship. Condition index (CI) is an instantaneous measure of environmental quality, whereas growth rates are an integrated measure of environmental conditions over an observed or simulated period (Filgueira et al., 2013). In experimental and modeling studies of bivalves, CI is often estimated using the meat content of an oyster. By explicitly modeling both shell and tissue biomasses, discrete values of simulated tissue can serve as a CI, while meat content is effectively simulated by the loss and accumulation of soft tissue at each model timestep. This addition makes ReefBioDES more suitable for aquaculture application, where farmers are interested in both harvest biomass and individual oyster quality. For leases that have not yet been established, the ability to model growth scenarios at different oyster densities using local water quality parameters and hydrodynamic data could prevent losses resulting from an unsustainable stocking density.

The lack of literature quantifying oyster growth and other physiological processes under commercial aquaculture conditions limits validation of simulated results. While the model simulations in this study effectively reproduced documented patterns of within cage food limitation and the resulting reduced oyster growth rates, analysis of the spatial and temporal trends of the highest density farm (800 oysters per cage) suggested that ReefBioDES may have overestimated the degree of food limitation created by filtration. Negative growth rates in the high-density simulation occurred frequently and in a large portion of cages (Fig. 18), causing oysters further away from the leading edge of the reef to be smaller at the end of the simulated period (Fig 18). Observations of the CBL aquaculture lease sampled as part of this study showed that 800 oysters per cage is a conservative cage density estimate, and stocking densities are typically much higher (>1000 per cage), especially for smaller oysters (>2000 per cage). Modelled growth rates were inversely related to oyster density and length. If the average growth rate on the high-density farm was 1.02 mm month^{-1} (less than half of all other simulations), increasing cage density would further reduce the modelled growth rate.

Oyster ploidy considerations may explain why oysters in the high-density simulation, which was more representative of an aquaculture site, began losing biomass. The bioenergetic formulas incorporated into ReefBioDES were originally formulated to model oysters on a natural reef (Cerco, 2015), which would be diploid. Local studies have reported *C. virginica* growth time to market size (76mm in Virginia) in diploid and triploid oysters of 1.5 and 1.2 years, respectively (Harding, 2007). Although growth rates are not linear across an oyster's life, even a rough extrapolation of this triploid growth rate, ~4.16 mm $month^{-1}$, is much higher than all model simulations, which ranged from 1.02 to 2.48 mm $month^{-1}$. Alternatively, Bodenstein et al. (2021) observed growth of *C. virginica* in response to experimental stress treatments meant to simulate conditions on an bottom cage aquaculture farm in the Gulf of Mexico, where tumbling oysters to sort them and/or to improve shell shape is common practice (Ring, 2012). Diploid and triploid oysters were both studied and had average growth rates of 0.16 and 0.23 mm d^{-1} (4.8 to 6.8 mm $month^{-1}$), respectively, which were higher than modeled in the simulations. Reported measurements directly from an aquaculture site are uncommon and this study provides some insights for comparison; however, these measures may not be representative of oyster growth in the Chesapeake Bay.

Assessing oyster aquaculture as a nutrient management strategy

Modelled estimates of denitrification were generally lower than comparable field studies. Humphries et al. (2016) measured seasonal denitrification rates at an aquaculture site (~700 oysters m^{-2}) and a restored reef (~54 oysters m^{-2}) in Rhode Island (USA), where mean denitrification rates (±SE) were higher at the restored reef than the aquaculture site, 581.9 (±164.2) and 346 (±168.6) μmol N_2–N m^{-2} h^{-1}, respectively. These values are some of the highest ever reported for an oyster community, and 2-4 times higher than the summer peaks from model simulations (~130-170 μmol N_2–N m^{-2} h^{-1}). Higgins et al. (2013) measured seasonal denitrification rates at 2 floating aquaculture sites and reported mean denitrification (± SE) rates of 0.69 ± 0.31 and 0.96 ± 0.24 mmol N m^{-2} d^{-1} at each of the two sites.

Modelled denitrification rates remained low compared to literature values but were higher than typical bare estuarine sediments in low-nitrate environments (J. Testa et al., 2015) (Testa et al. 2015). The reef scenario in this study simulated denitrification rates comparable to the high-density farm scenario, as might be expected based on comparable biodeposition rates. Other mechanisms of oyster-mediated N removal have been documented that were not modelled in ReefBioDES. For example, the shells of oysters have been shown to be sites of enhanced nitrification and denitrification, and living oyster shells were associated with significantly higher rates of denitrification (Caffrey et al., 2016). Shellfish aquaculture environments are characterized by high densities of individuals, compared to natural environment, potentially increasing the available shell surface area for enhanced microbial denitrification. The additional gear used in bottom cage aquaculture operations, such as the bags which contain oysters, may provide an alternative site for biodeposition thereby decreasing the benthic flux of organic matter. There is also evidence of anoxic microsites within the aerobic layer which may enhance coupled nitrification and denitrification (Jenkins & Kemp, 1984; Jørgensen, 1977). Each of these processes may increase the N removal potential of aquaculture environments in a way not modelled in this study.

Model results of N removal associated with denitrification, burial, oyster shell and oyster tissue are somewhat inconsistent with another large scale model used to estimate N and P removal of restored oyster reefs. Kellogg et al. (2018) modelled the restored reefs of Harris Creek M.D. to estimate annual N removal via each of the aforementioned mechanism. N removal in the Harris Creek model is dominated by denitrification, followed by sequestration in shells, sequestration in shells, tissue, and burial. Model simulations in this study showed similar rates of N removal via denitrification and tissue assimilation, followed by burial, and finally shell sequestration. A key difference between the simulations presented here and the estimates of Kellogg et al. (2018) are that Harris Creek denitrification losses were based on whole-reef incubation experiments that measure denitrification rates that were often an order of magnitude (~1200 mmol m^{-2} h^{-1}) greater than those modeled here. For all simulations performed with ReefBioDES, N burial was also higher than comparative studies of restored reefs, which used a 10% factor to convert from oyster biodeposits to nitrogen burial (Newell et al., 2005), as applied in the Kellogg et al. (2018) model. If that conversion factor was applied to modelled biodeposit production of ReefBioDES, N burial estimates would have been significantly reduced, but the dynamic calculation of burial predicted by the model may be a more realistic approach, given its ultimate dependence on biodeposit production rate *and* resuspension and deposition patterns within a complex bottom topography.

All model simulations had relatively high ammonium fluxes compared to both the bare sediment simulation and to typical sediments in the Chesapeake Bay, where ammonium fluxes of this magnitude have only been observed in hypoxic sediments. These results are consistent with other studies of oyster reefs (M. Kellogg et al., 2013) and aquaculture operations (Higgins et al., 2013; Mazouni et al., 1996) that have found high rates of ammonium fluxes associated with oyster communities, but the magnitude of ammonium fluxes in this study were much higher. Lunstrum et al. (2018) conducted a seasonal in-situ analysis of denitrification, dissimilatory nitrate reduction to ammonium (DNRA), and dissolved inorganic N fluxes at a rack and bag aquaculture site in the Chesapeake Bay and found similarly high rates of ammonium efflux, with peak summer values of 935 μmol m^{-2} h^{-1}. These observations fall somewhere in between modelled ammonium fluxes at the large farm and high-density farm/reef, where fluxes peaked at ~800 and ~1200 μmol m^{-2} h^{-1}, respectively. Water column measurements of ammonium were comparatively lower, which the authors attributed to high flushing rates. The mean water depth was 1.1m and the racks sat ~30cm off the sediment surface, which more closely resembles the cages observed and modelled in this study, where the mean water depth was ~0.9 m and there was a ~10 cm space under each cage, compared to studies of floating aquaculture. Remineralization of settled oyster biodeposits is shown to increase rates of ammonification, which may increase ammonium concentrations in the water column and provide a source of inorganic N for primary producers (Dame, 2016). Flushing rates and oyster density must both be considered in determining what effect ammonium efflux will have local water quality and subsequent N transformations.

The iteration of ReefBioDES applied in this study is capable of simulating oyster growth and nitrogen cycling on aquaculture farms using site-specific forcing data which are relatively easy to obtain. Water quality parameters including chlorophyll, temperature, and salinity and site characteristics such as depth, sediment grain size, and composition could all be discretely measured and used to force ReefBioDES. It may also be useful to measure the ratio of chlorophyll to TSS, a conversion factor which is used at multiple points in the model as simulated particle transport interacts with oyster filtration and bioenergetics. The simulations in this study used measurements from the tidal survey of the CBL aquaculture lease to calculate this parameter.

Thus far, temporal variation and lack of access to site-specific measurements of N removal have prevented the inclusion of indirect N removal processes in oyster aquaculture crediting schemes. ReefBioDES may offer a way to expand nitrogen credits by quantifying N removal processes of an individual aquaculture farm using easy to obtain observational data. In model simulations, oyster density and farm size determined oyster growth and biodeposition rates, which controlled nutrient cycling. While model results from smaller, lower density farms had higher rates of denitrification and growth, biomass yields were relatively low and, consequently, so was N removal via bioextraction. The large farm scenario represented an intermediate case where denitrification and oyster growth were maximized. Modelled N removal via indirect processes (denitrification and N burial) suggest there may be increased potential for oyster aquaculture operations to be adapted as a nutrient management strategy; however, simulations with oysters also saw high ammonium fluxes that have implications for the net N removal potential of an aquaculture farm. The rates of denitrification on farms simulated in this study were relatively low compared to (limited) field experiments of bottom cage oyster aquaculture leases, but simulated farms had higher rates of N removal than the bare sediment simulation. Calculations of N removal for nitrogen crediting purposes should consider lease-specific configurations and environmental parameters.

Model limitations and future considerations

Much attention was given to the calculation of ingestion in this study and the associated parameters could benefit from further analysis and sensitivity testing. Removal of chlorophyll from the water column via filtration, oyster growth, and biodeposition are all modelled using an ingestion rate formulated from a comparative study of oyster biodeposit production (Cerco, 2005), where the ingestion capacity of an oyster increases with TSS concentration and reaches a maximum at 4mg L^{-1} (*Imax*). The rate of biodeposit production ultimately determines how much organic matter is sent to SFM for subsequent transformation. If *Imax* was set to a higher value, oyster growth and biodeposition rates would have increased and more N would have been shunted to the sediment community, further increasing ammonification in most scenarios.

Additionally, modelling ingestion as a maximum rate assumes that a) all ingested material has the same energy content and b) all filtered material is removed via pseudofeces production or ingestion and none remains in the outflow of water. Regarding the first assumption, oysters have demonstrated preferential ingestion of organic rich particles (Newell & Jordan, 1983) and selective feeding between different phytoplankton taxa (Ward & Shumway, 2004; Weissberger & Glibert, 2021). So, while this study uses a fixed conversion of grams of seston (TSS) to joules of energy (1:22,000; Cerco, 2015), local water quality parameters and season may influence the taxonomic composition of seston, resulting in a dynamic relationship between the amount of seston an oyster filters and the energy provided in that material. Similarly, the factor used to convert biodeposits to mg of PON is based upon studies from the Choptank River (Jordan, 1987). Increasing the value of this parameter would also increase the N delivered to the benthos.

Several of the aforementioned limitations surrounding the calculation of oyster ingestion could be improved by incorporating a nutrient–phytoplankton–zooplankton–detritus (NPZD) model into the advection-diffusion model of ReefBioDES. First, an NPZD model could simulate a dynamic food source for oysters to selectively ingest and reject as pseudofeces, which would allow for variation in the energy density of ingested material. For example, upstream oysters may preferentially ingest nutrient-rich seston thereby stimulating growth. Depending on the magnitude of downstream chlorophyll depletion and variation between the energy content of different food sources, downstream oysters may experience more or less food limitation than was observed in this study. Because pseudofeces, the primary component of biodeposits, were calculated as the difference between filtered and ingested material, changing the composition of ingested material would also change the chemical makeup of the biodeposits which force N transformations in the sediment-water chemical flux model. Finally, nutrient fluxes from the benthos could serve as input to the NPDZ model, creating feedback between sediment and water-column chemistry that does not currently exist in ReefBioDES.

As seen in the field observations of oyster size and density at the CBL lease, aquaculture farms are comprised of several size (age) classes of oysters so that growers can harvest at market size more frequently than the oyster’s full 18-24 month grow out period (for triploid oysters, Parker et al. 2020). Physiological processes like those modelled here, namely filtration and growth, vary with age, and the simulations performed here did not capture any consequences that may result from having a wide range of oyster sizes on a farm. Although all oysters in these simulations were parameterized with a time zero weight of 1 gDW, it is possible to have several size classes of oysters on the farm leveraging the current model domain of grid cells which model chlorophyll movement and simulate filtering oyster. Such simulations may be useful to growers to find a farm configuration that maximizes oyster growth. In this study, oysters were simulated as only filtering from the bottom grid cells of the model domain, which effectively concentrates the effect of particle removal and food availability to cells ~2.5 cm^{-2} . Future simulations could model filtration as occurring further up into the water column, which would be more representative of how oysters are distributed with cages.

These simulations also did not account for effects of oyster ploidy. As previously described, growth rates of triploid oysters are generally significantly higher than diploid oysters. Triploid oysters do not expend energy into reproduction, and so this process was not modelled. These initial simulations were aimed more at model development, and as such, it was important to keep simulation parameters constant except for the variable being tested (e.g., oyster density, farm length). Ideally, ReefBioDES could be further developed to represent the differences between triploid and diploid oysters for simulating aquaculture and reefs, respectively.

Validation of the sediment biogeochemical model results could be expanded using spring and summer 2021 and 2022 measurements of porewater concentrations, sediment nutrient concentrations, and sediment-water flux from the CBL aquaculture lease. Porewater samples measuring NO_3, NH_{4+}, PO_4, and sulfide were taken inside and outside of the farm footprint at select stations along the same sampling transect previously described. Sediment samples were also taken and analyzed for concentrations of particulate nitrogen and phosphorus. Additionally, ReefBioDES could be used to create a nitrogen budget for an aquaculture farm. By modeling the physical and biogeochemical processes that influence the fate of aquaculture-derived PON using mass balance equations, ReefBioDES can create an N budget that includes an input of total deposition (oyster-derived and background) and output of denitrification, burial, and export from the farm.

The implementation of the sediment flux model requires a 10-15 year "priming" period to allow sediment nitrogen and carbon stocks to stabilize relative to the local conditions. The priming period implemented in these model simulations only included background deposition without additional input from oyster biodeposits, effectively assuming the simulated aquaculture site had been present for only as long as the model simulations were run, which in this study is at most 5 months. Because long-term aquaculture sites may be more susceptible to the deleterious environmental effects sometimes associated with aquaculture (Burkholder & Shumway, 2011; Dumbauld et al., 2009), modeling long-term impacts of farms may be particularly important in systems with low current flow, in shallow water, and/or those with intense aquaculture operations. Future simulations should consider a priming period that adds POM from oysters to reflect the history of the farm.

This study did not look extensively at the effect of cage density and size, because cage dimensions on the observed and modelled CBL aquaculture lease showed little variation. Factors like accessibility by boat, especially at shallow sites, and the ability to lift and handle the cage for upkeep were assumed to restrict variation in cage spacing and size. However, several studies have demonstrated local effects of aquaculture gear on current flow associated with fish cages (Bi & Xu, 2018; Wu et al., 2014) and floating bivalve aquaculture. Zhao et al. (2015) conducted experiments to quantify differences in velocity flow between several multi-cage configurations of fish net cages, in a steady current. Results demonstrated that cage arrangements can be optimized to increase current velocity. Such hydrodynamic considerations have important implications for oyster growth and survival, stocking densities, and local biogeochemistry (Campbell & Hall, 2019). There is much diversity in shellfish aquaculture gear types, and the simulated farm and reef scenarios in this study suggest that such hydrodynamic differences significantly influence both the nutrient reduction capabilities of an oyster population (i.e., N removal), and harvest potential (i.e., growth).

As with previous iterations of ReefBioDES, model results suggest that a nuanced relationship between oyster density, biodeposit resuspension frequency, and farm length will affect the indirect N removal potential of an oyster community. This latest iteration of ReefBioDES demonstrates that the spatial distribution of oysters (i.e., reef or farm) is likewise important, while also providing valuable new insights into oyster growth and the associated direct N removal. The products that result from modelling efforts like this study can be useful to fill knowledge gaps when experimental data is difficult to obtain. While this study has identified ways in which ReefBioDES could be improved, there is potential for this model to be useful for growers to predict potential nitrogen credits when fully developed with a user interface.

Tables

Coefficient	Estimate
β_0	-0.7459
β_1	0.1478
β_2	$-4.21E^{-3}$
β_3	$2.55E^{-4}$
β_4	$-5.21E^{-6}$

Table 1. Coefficients for the Jordan (1987) formulation of biodeposit production (mg gDW^{-1} hr^{-1}) parameterized for *C. virginica*.

simulation	oysters per cage	number of cages	farm length (m)	effect
1	300	20	35	small farm
2	300	40	70	large farm
3	800	30	50	high-density
4	200	30	50	low-density
5	170 oysters per m^2 and 70 m long			reef

cage height (h)	cage width (b)	cage length (l)	space between cages (s_x)	initial oyster weight (gDW)	shell length (cm)
0.75	1.0	1.0	0.75	1.0	~6.30

Table 2. Details of the 5 long-term simulations, including oyster density, number of cages (for farms), length of farm/reef, and variable being tested. The oyster metrics, standard cage dimensions, and spacing used in all simulations are also listed.

	Farm size		Farm density		Reef
	small	large	low	high	
Growth rate (mgDW d^{-1})	2.39	2.20	2.55	1.02	1.58
Growth rate (mm $month^{-1}$)	2.34	2.16	2.48	1.02	1.58
Final shell length (cm)	7.17	7.10	7.22	6.68	6.89
Biodeposition rate (g m^{-2} h^{-1})	4.28	3.90	3.03	7.02	5.15
N (oysters per m^2)	171.43	171.43	114.29	457.14	170.00
Farm/reef length (m)	35	70	50	50	70

Table 3. Summary table of key bioenergetic output from the 5 long-term model simulations. Oyster density (m^{-2}) and farm/reef length is also given for reference. All oysters weighed 1gDW (shell length ~6.30 cm) at the beginning of a simulation. Biodeposition and gDW of tissue growth are both explicitly modelled, and shell length was calculated using an empirical formula for triploid oysters (gDW = 0.00005*(mm shell length)$^{2.39}$; Cornwell et al., 2016).

	Farm size		**Farm density**		**Reef**
	small	large	low	high	
ΔN in tissue (g N)	174.27	319.87	182.95	294.03	232.51
ΔN in shell (g N)	8.99	17.67	8.98	30.82	16.83
Denitrification (g N)	150.40	282.40	213.55	191.82	251.71
Burial (g N)	56.48	116.13	81.91	90.51	126.11
Biodeposition (kg N)	106.32	196.11	105.52	244.26	213.20
Oyster density (m^{-2})	171.43	171.43	114.29	457.14	170
Reef/farm length (m)	35	70	50.75	50.75	70
Initial biomass (g)	5880	11760	5800	23200	11900

Table 4. Summary table of estimated direct (tissue and shell) and indirect (denitrification and burial) nitrogen removed during each simulation, and several parameters that may influences these rates including: total biodeposit production during a simulation (kg N), across farm oyster density (m^2), reef/farm length (m), initial oyster biomass (g), and initial total oyster count across the farm. The ΔN values in shell and tissue were calculated using the sum of tissue/shell that accrued during the simulation period, discounting their initial weight.

Figures

Sampling stations and ADCP/EXO2 deployment across studied aquaculture lease

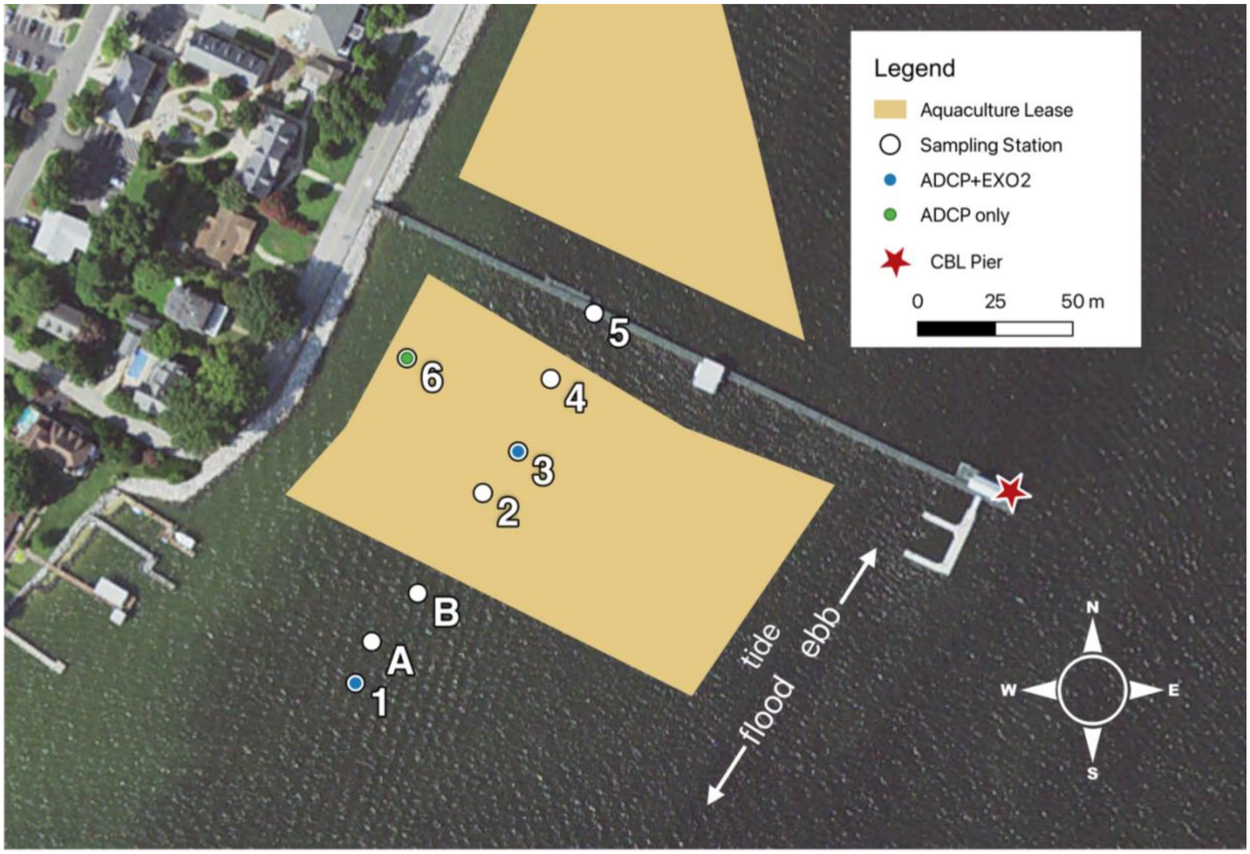

Figure 1. Aerial view of the aquaculture lease sampled for forcing and validation data, located off Solomons Island, Maryland, U.S.A. The primary sampling transect was comprised of the 7 stations running through the middle of the farm, 3 of which were contained inside the farm and 4 of which were outside the farm. The red star represents the CBL long-term monitoring station where forcing data for longer simulations were obtained.

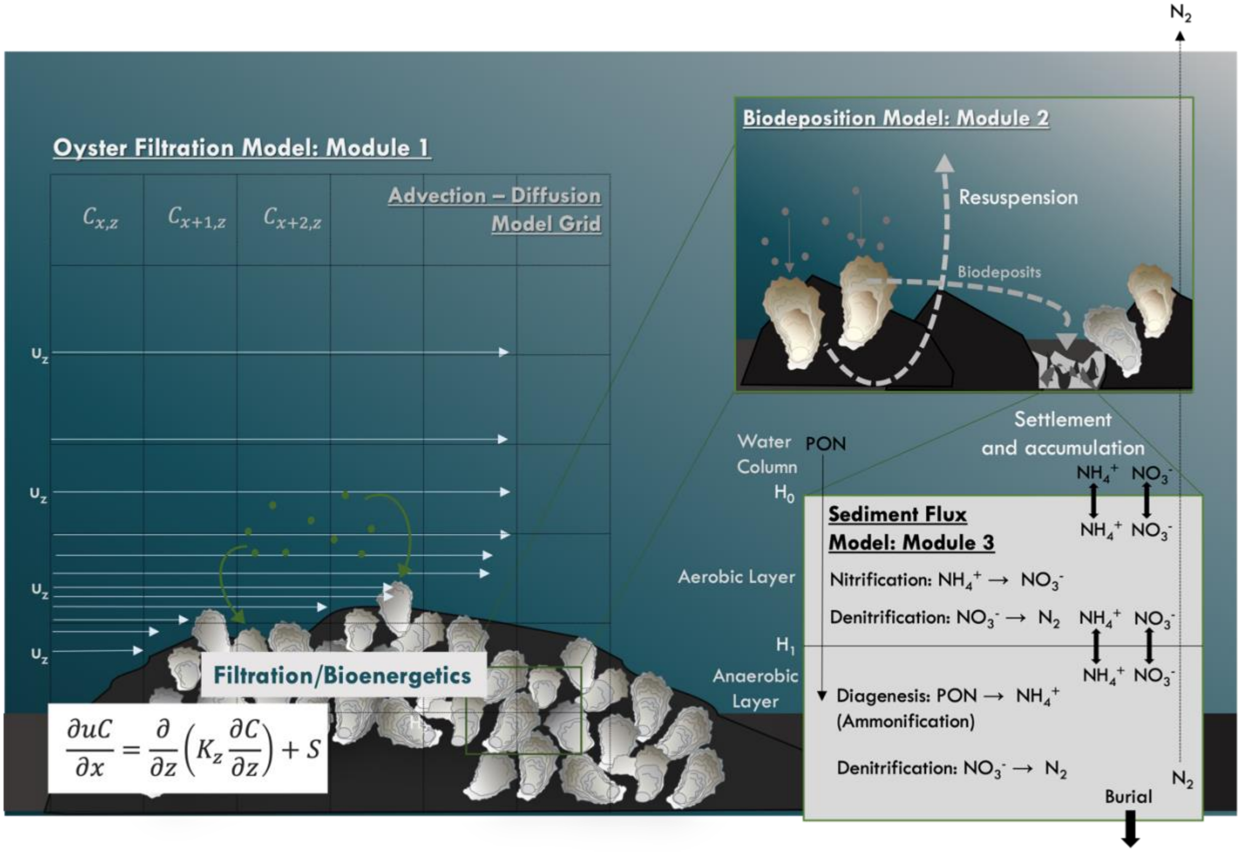

Figure 2. Conceptual diagram depicting the three modules that comprise ReefBioDES including the advection-diffusion and bioenergetics models (Module 1), biodeposit transport model (Module 2), and sediment flux model, SFM (Module 3).

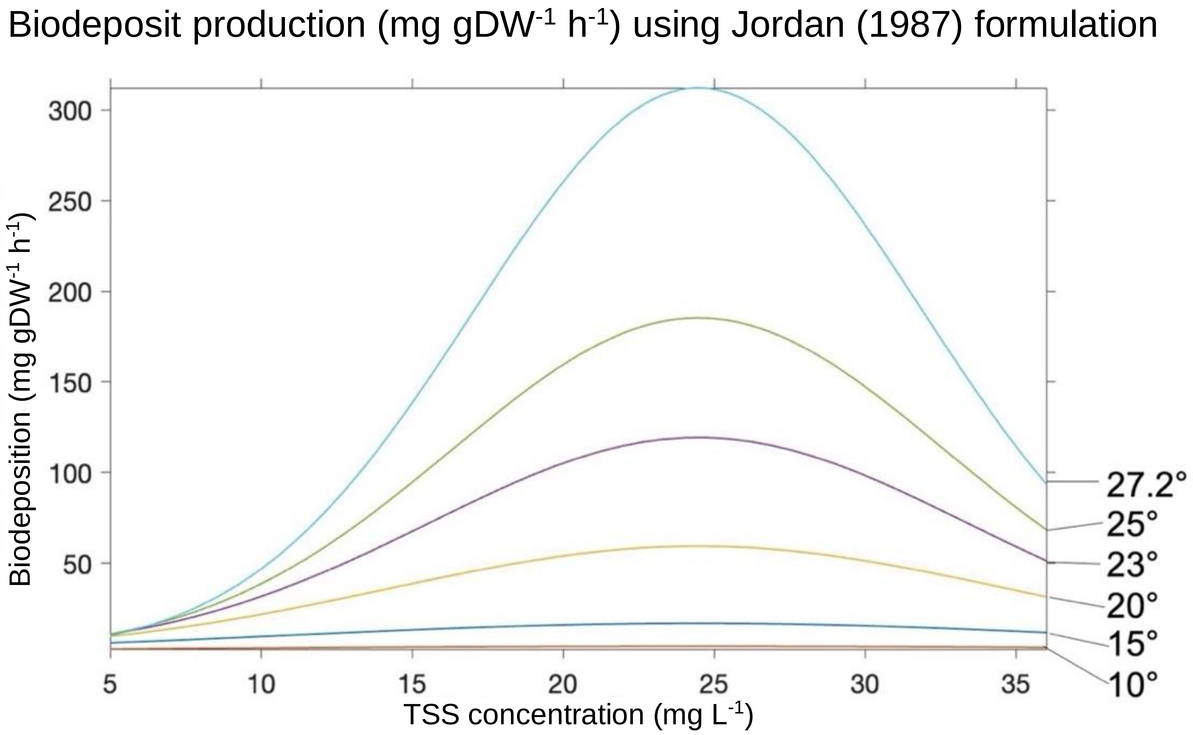

Figure 3. Plot of biodeposition rates (mg gDW^{-1} hr^{-1}) over a TSS concentration of 5 to 35 mg L^{-1}. Each line represents biodeposit production rate at a different temperature where 27.3℃ is the maximum biodeposition rate at a given TSS concentration (adapted from Jordan, 1987).

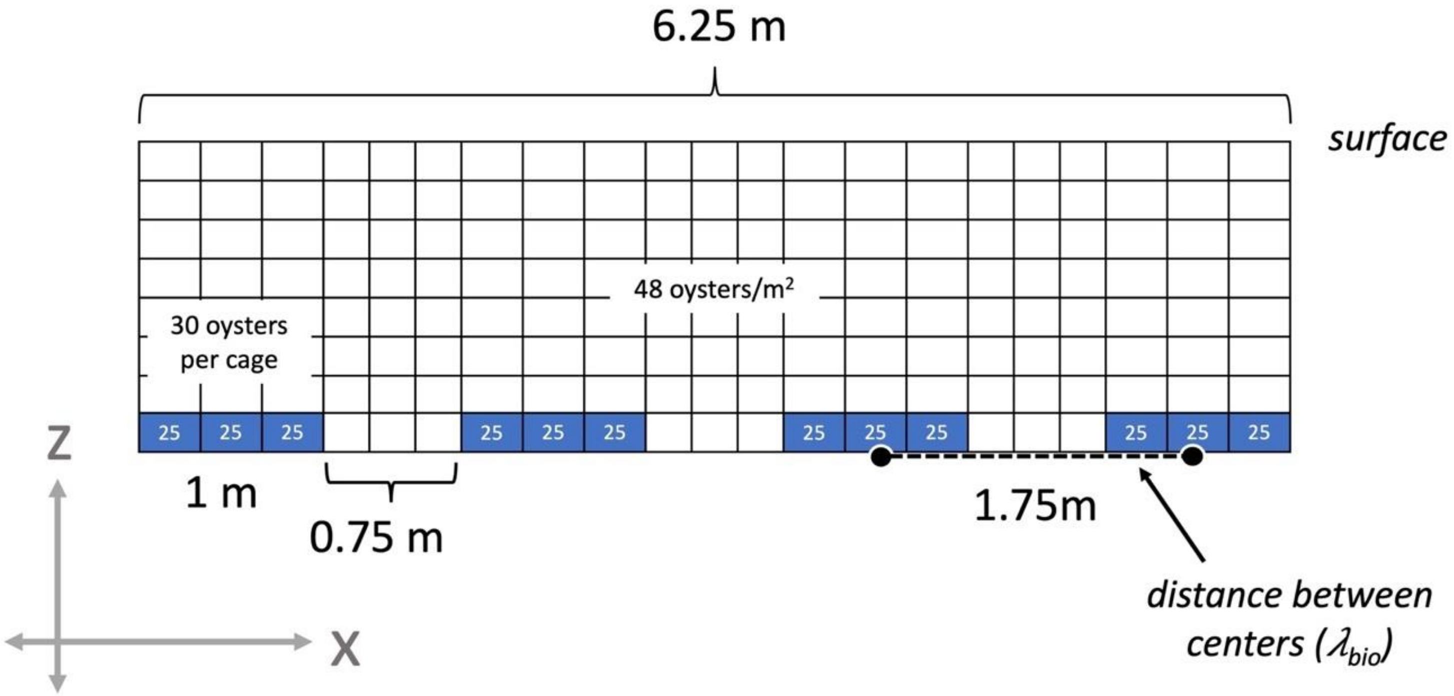

Figure 4. A user input density of 75 oysters per cage, cage length of 1 m, spacing of 0.75 m, and 4 cages will produce the above spatial domain. Note that the actual model would typically have a cell length of ~ 2.5 cm, yielding hundreds of cells containing 5-10 oysters per cell, depending on the parameters of each simulation.

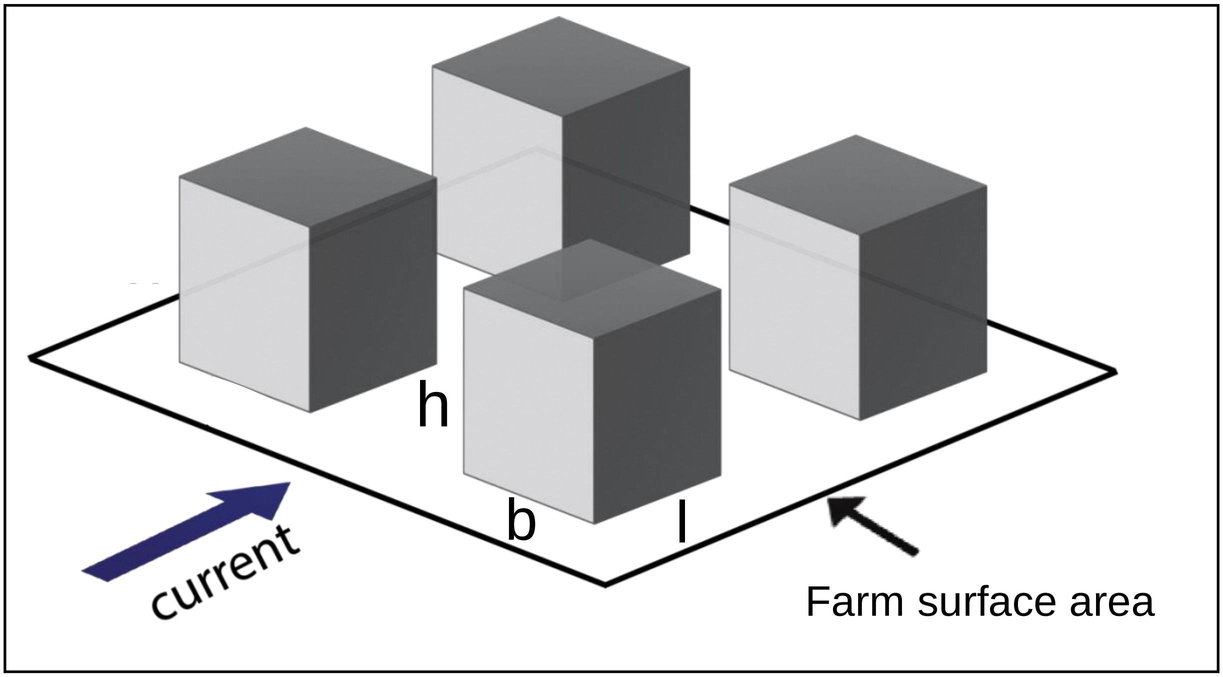

Figure 5. Conceptualization of cages as equally spaced roughness elements (*n* = 4) over a plane. Height *h* and base *b* are, by definition, perpendicular to the current flow and length *l* is parallel to the current. Farm surface area *S* is the sum of reference areas for all cages, which includes the projected basal area of all cages defined. Basal projected area is the product of *b* and *l* , extrapolated to the entire farm using multiplier *n*.

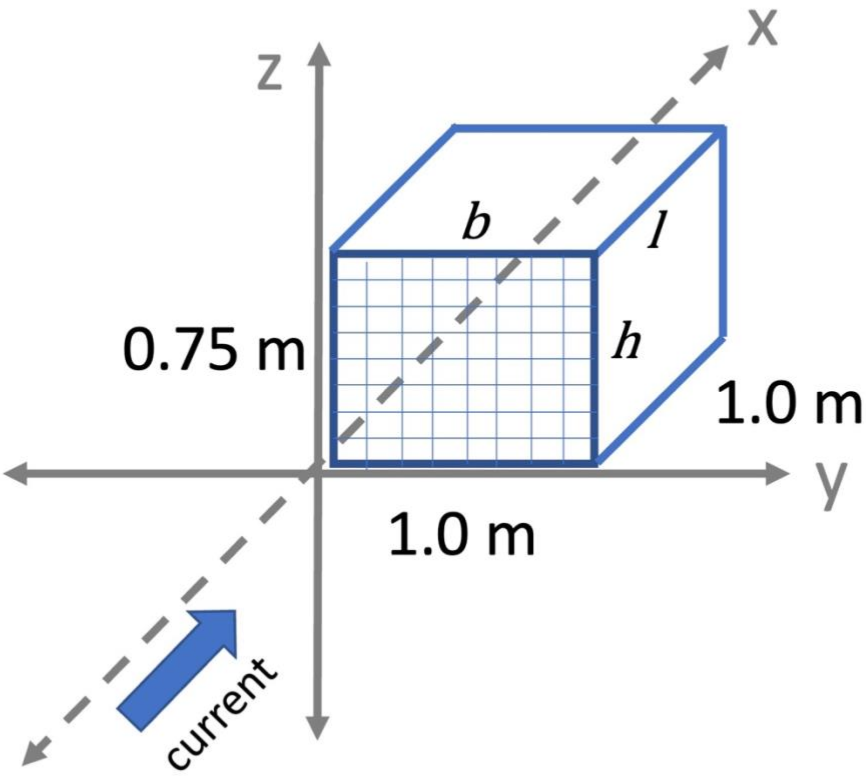

Figure 6. Diagram of a simulated aquaculture cage with a base (*b*) and length (*l*) of 1.0 m and height (*h*) of 0.75 m. Current approaches the face of the cage in the x direction.

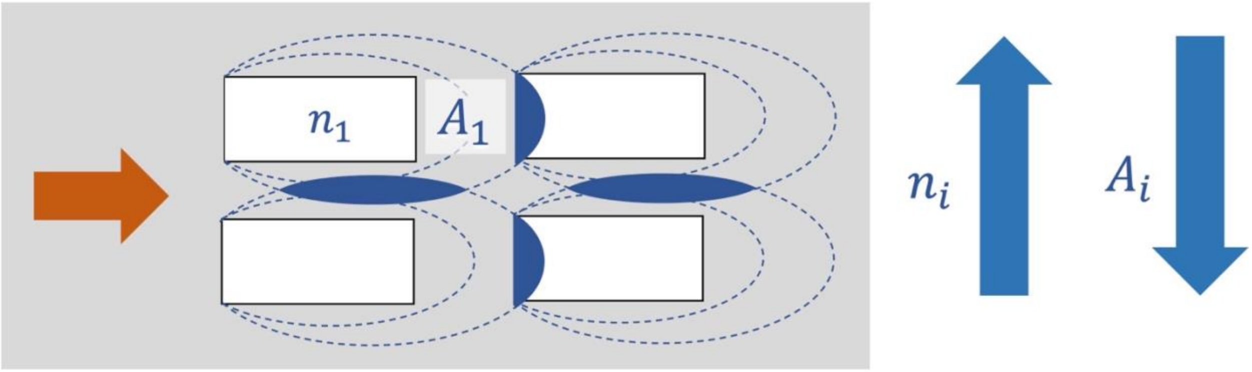

Figure 7. Top view of multiple roughness elements interacting with each other. The effective shelter area is represented by A_i. As the number of roughness elements (n) increases, the individual effective sheltering area decrease. Adapted from Shao and Yang (2005).

Mid-farm CHLA concentrations (µg L^{-1}) in summer (2021): modelled and observed

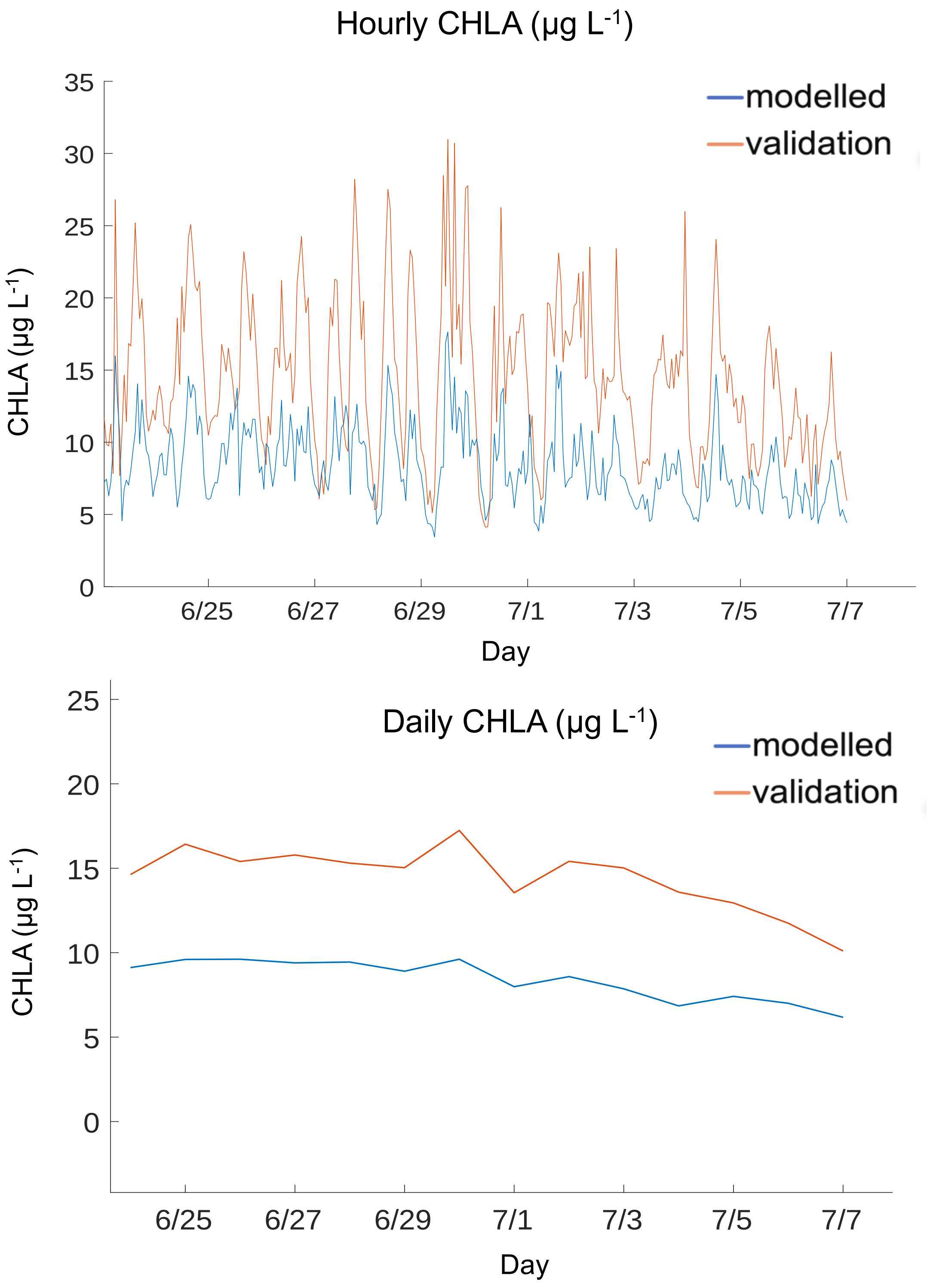

Figure 8. High frequency (15 minute) CHLA concentration (μg L^{-1}) data from a mid-farm sampling station compared to an extraction of modelled mid-farm CHLA plotted at hourly (top) and daily (bottom) timesteps. Data collected outside of the farm during the same 2-week summer period (July 2021) were used to force the initial 2-week model simulations.

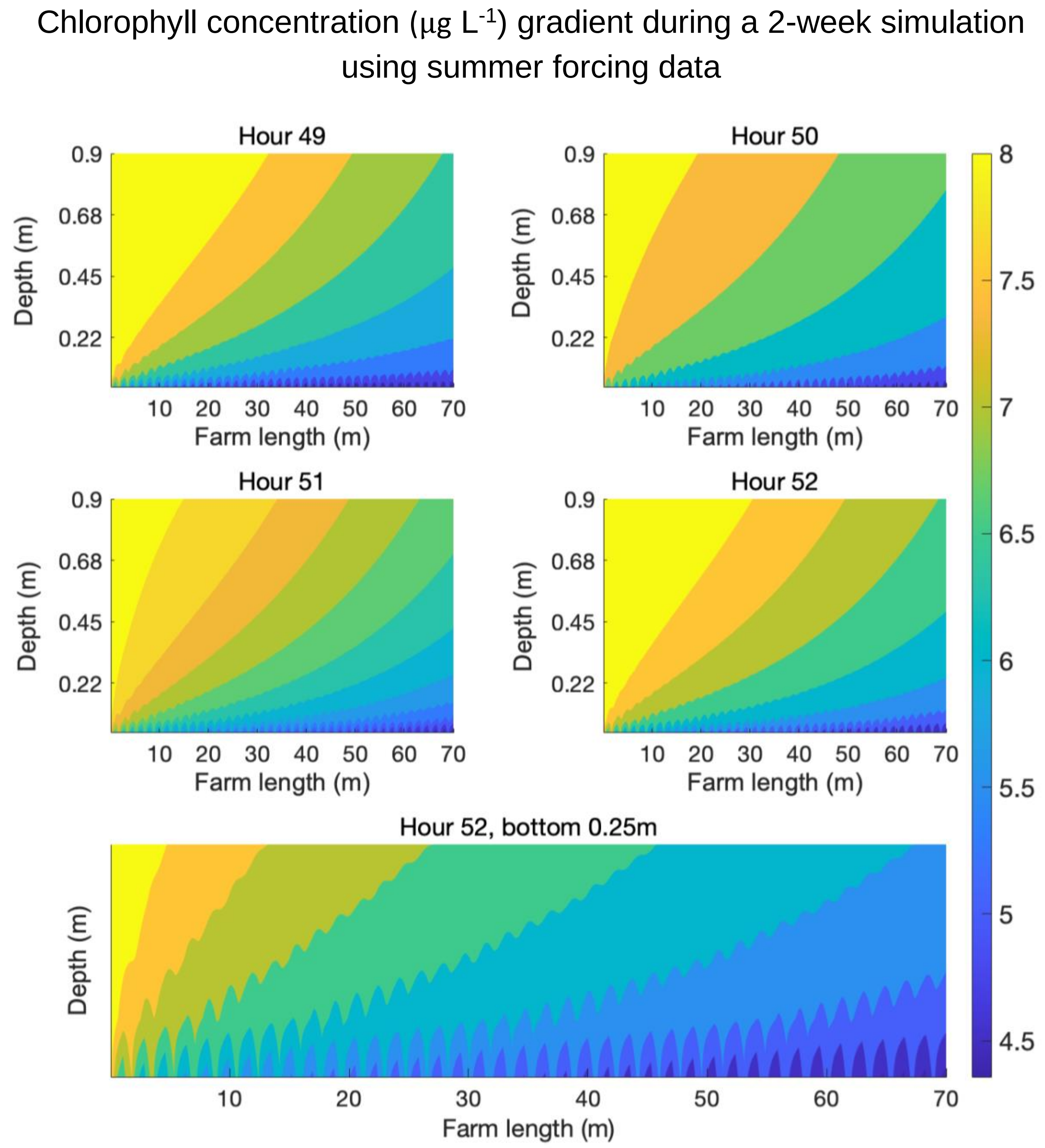

Chlorophyll concentration ($\mu g\ L^{-1}$) gradient during a 2-week simulation using summer forcing data

Figure 9. Chlorophyll concentration ($\mu g\ L^{-1}$) during day 2 (hours 49, 50, 51, and 52) of a 2-week simulation forced with temperature, salinity, DO, CHLA, and velocity data collected at the leading edge of the aqaucutlure farm (July 2021). The bottom panel is the CHLA at hour 52 magnified to show the bottom 0.25 m of the water column.

Chlorophyll concentration (μg L^{-1}) collected at the study aquaculture lease

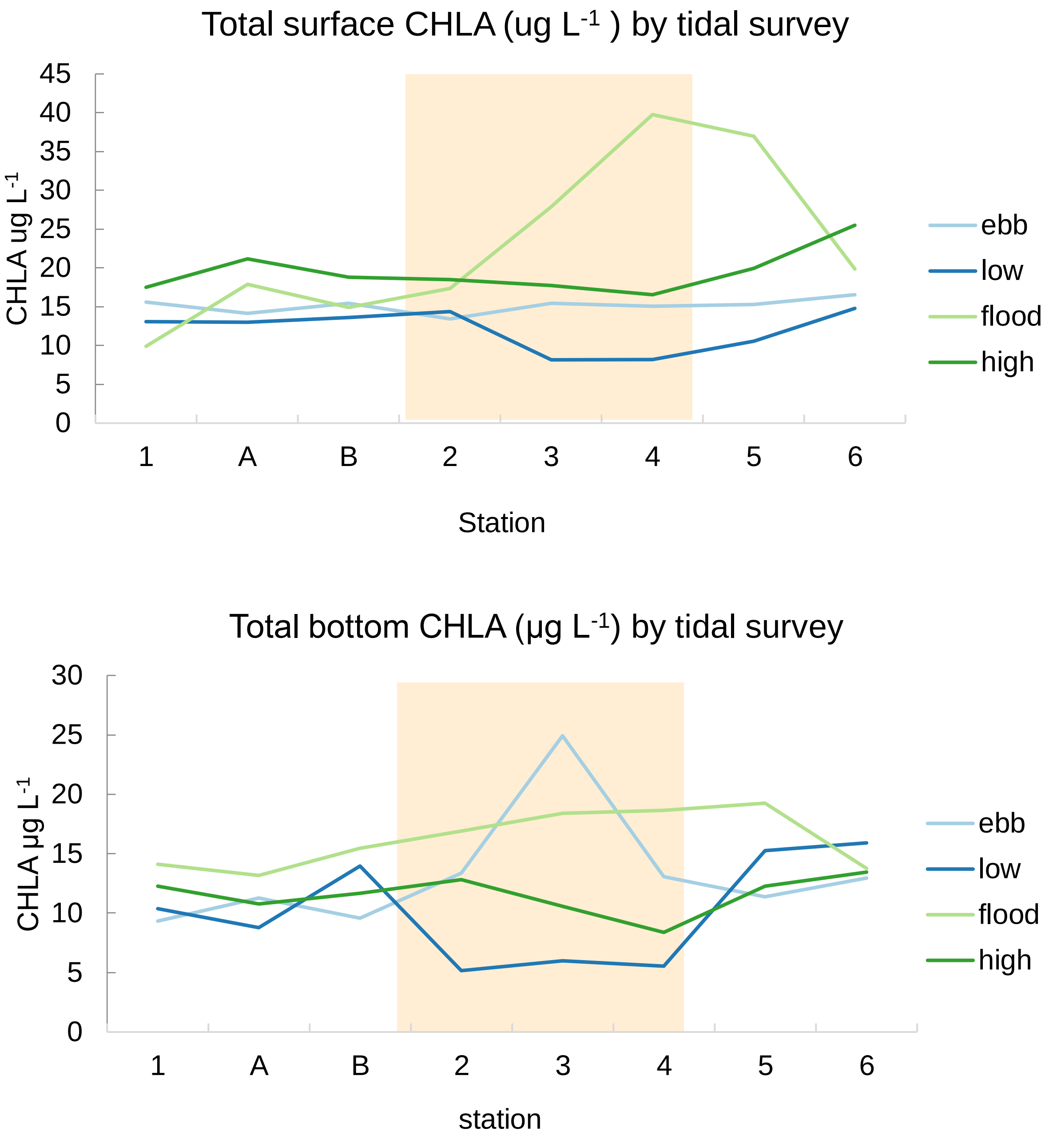
Total surface CHLA (ug L^{-1}) by tidal survey

Total bottom CHLA (μg L^{-1}) by tidal survey

Figure 10. Total chlorophyll concentration (μg L^{-1}) at each station plotted by tidal survey at the surface (a) and bottom (b) with data obtained during the summer sampling efforts. The shaded region denotes within farm stations 2,3, and 4.

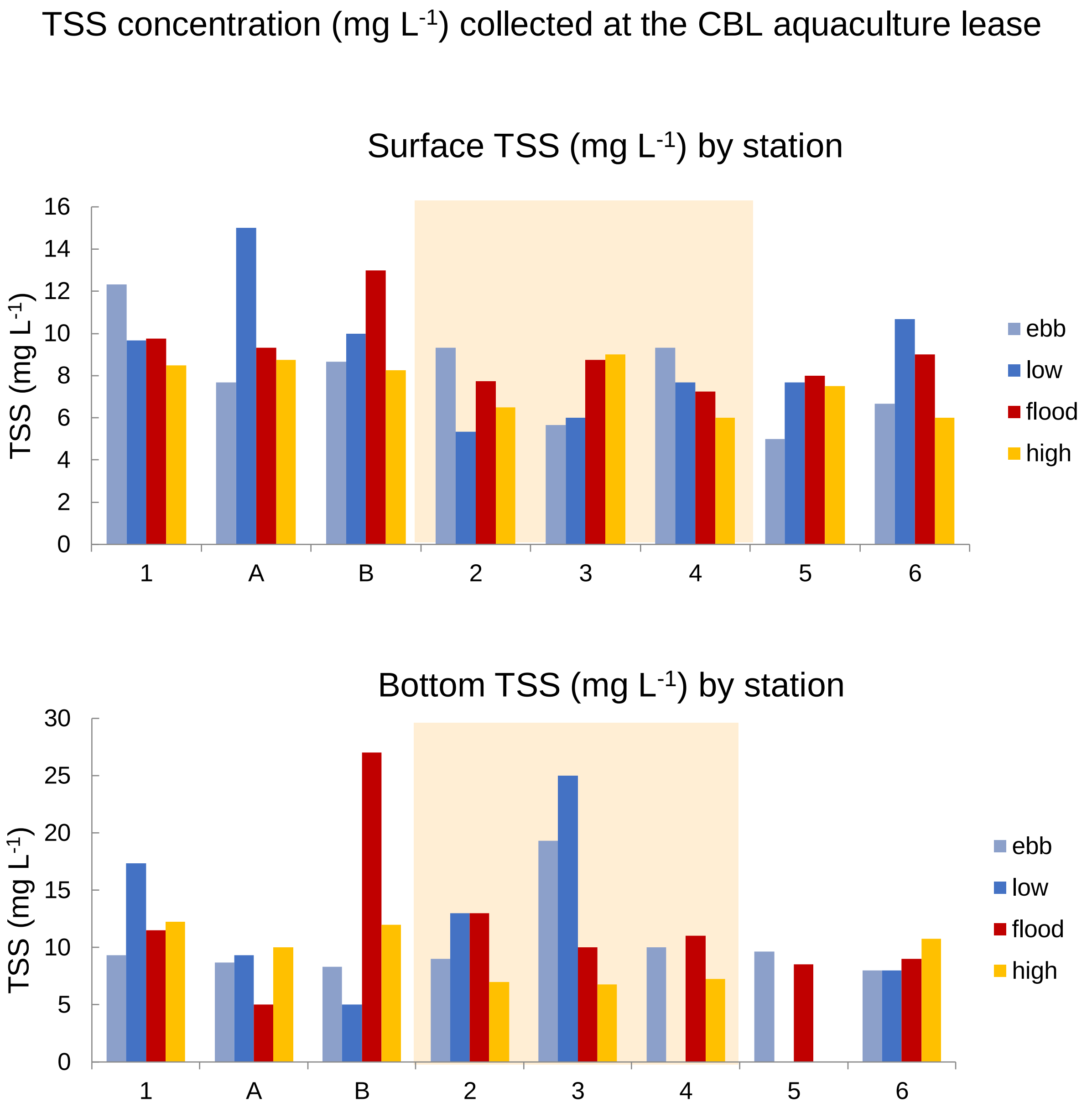

Figure 11. Surface and bottom water samples of TSS (mg L^{-1}) collected during the tidal survey. Missing samples for bottom water indicate ripped filters (station 4, survey 2; station 5, surveys 2 and 4). The shaded region denotes within farm stations 2,3, and 4.

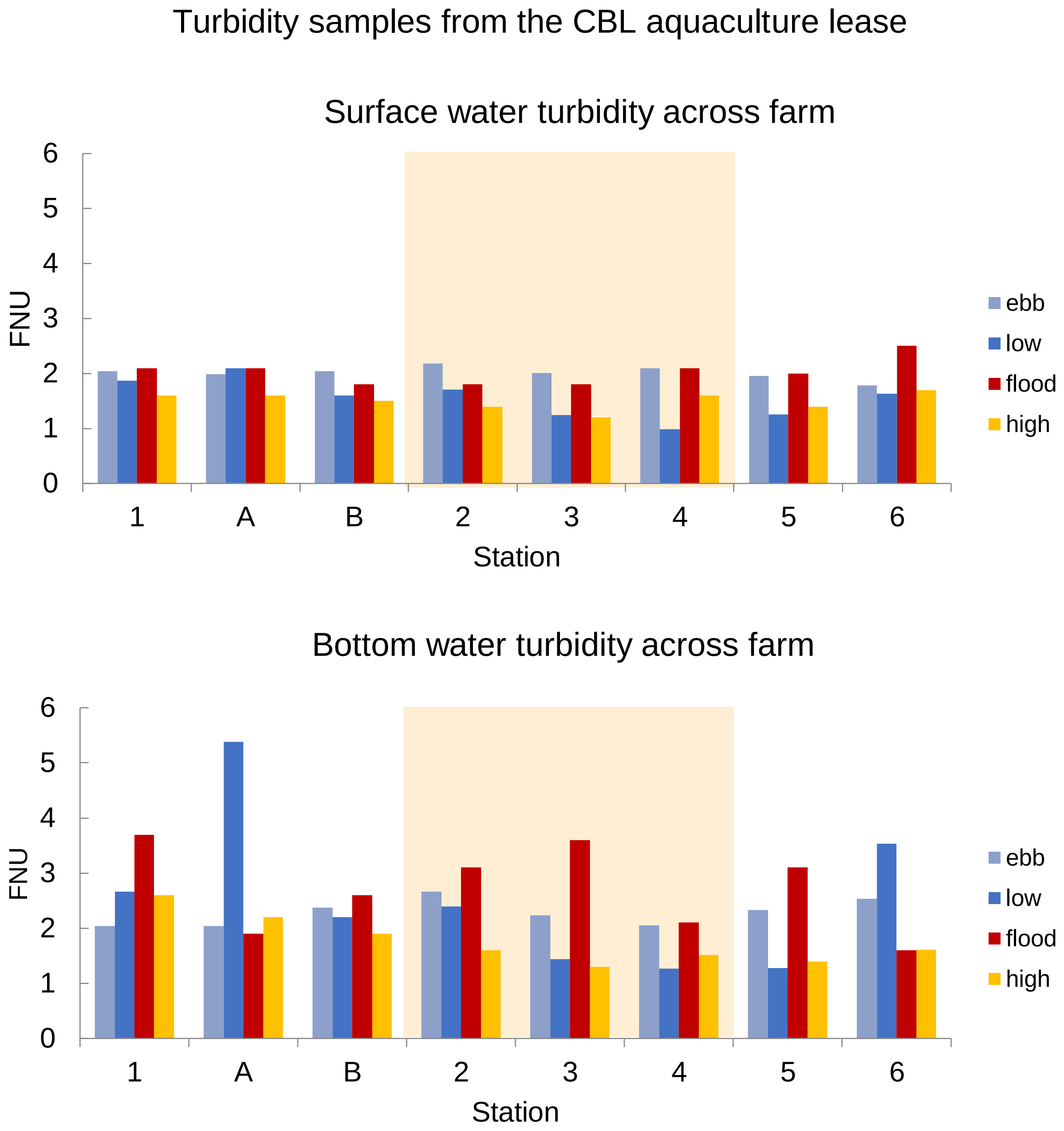

Figure 12. Turbidity samples (FNU) taken from surface and bottom water using the YSI EXO2 sondes. Samples were taken at each station for all surveys. The shaded region denotes within farm stations 2,3, and 4.

Modelled and observed current velocity (m s^{-1})

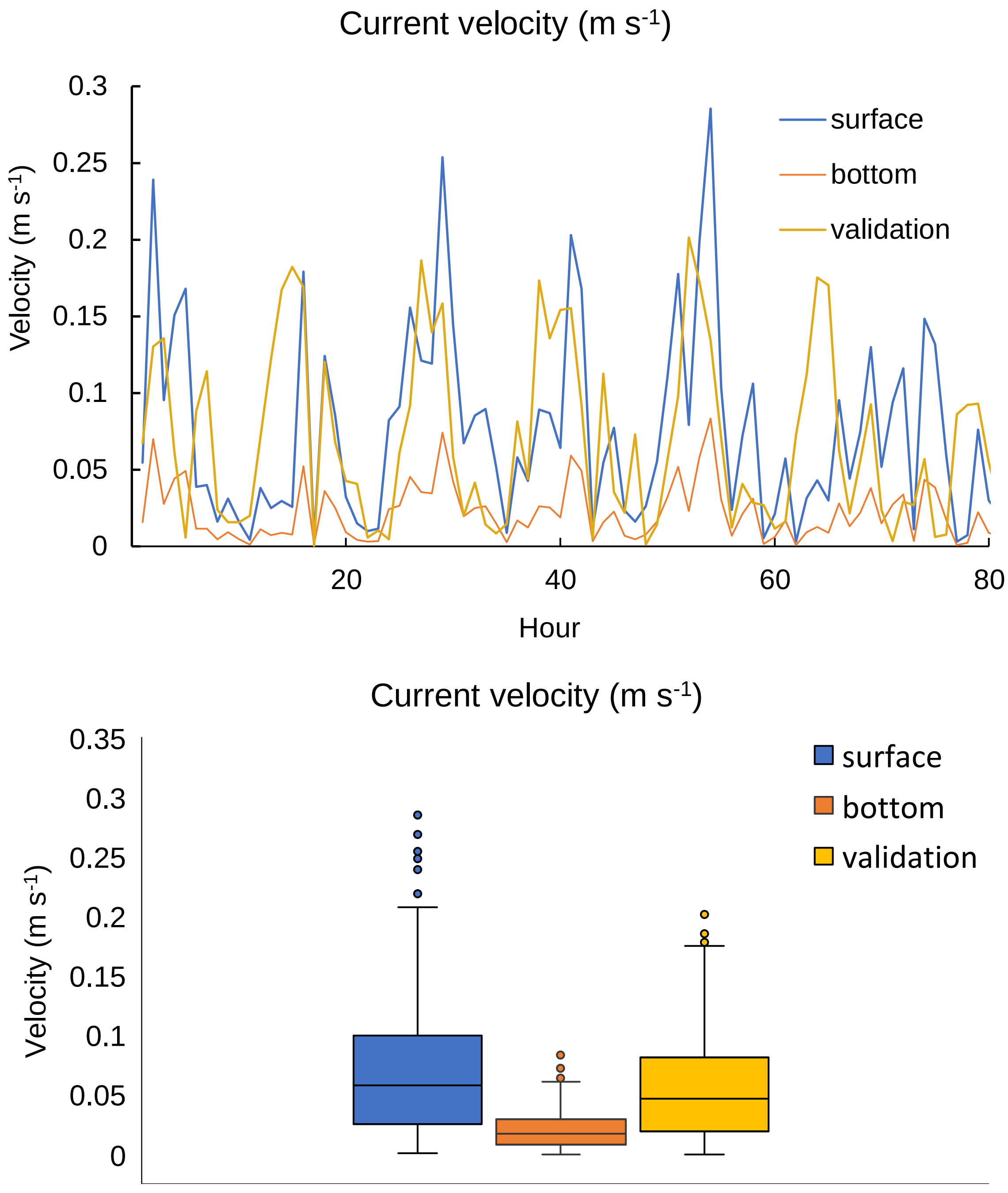

Figure 13. Hourly velocity data from the mid-farm spring platform (yellow) and model estimated velocity profile from the bottom most grid cell (orange) and the topmost grid cell (blue).

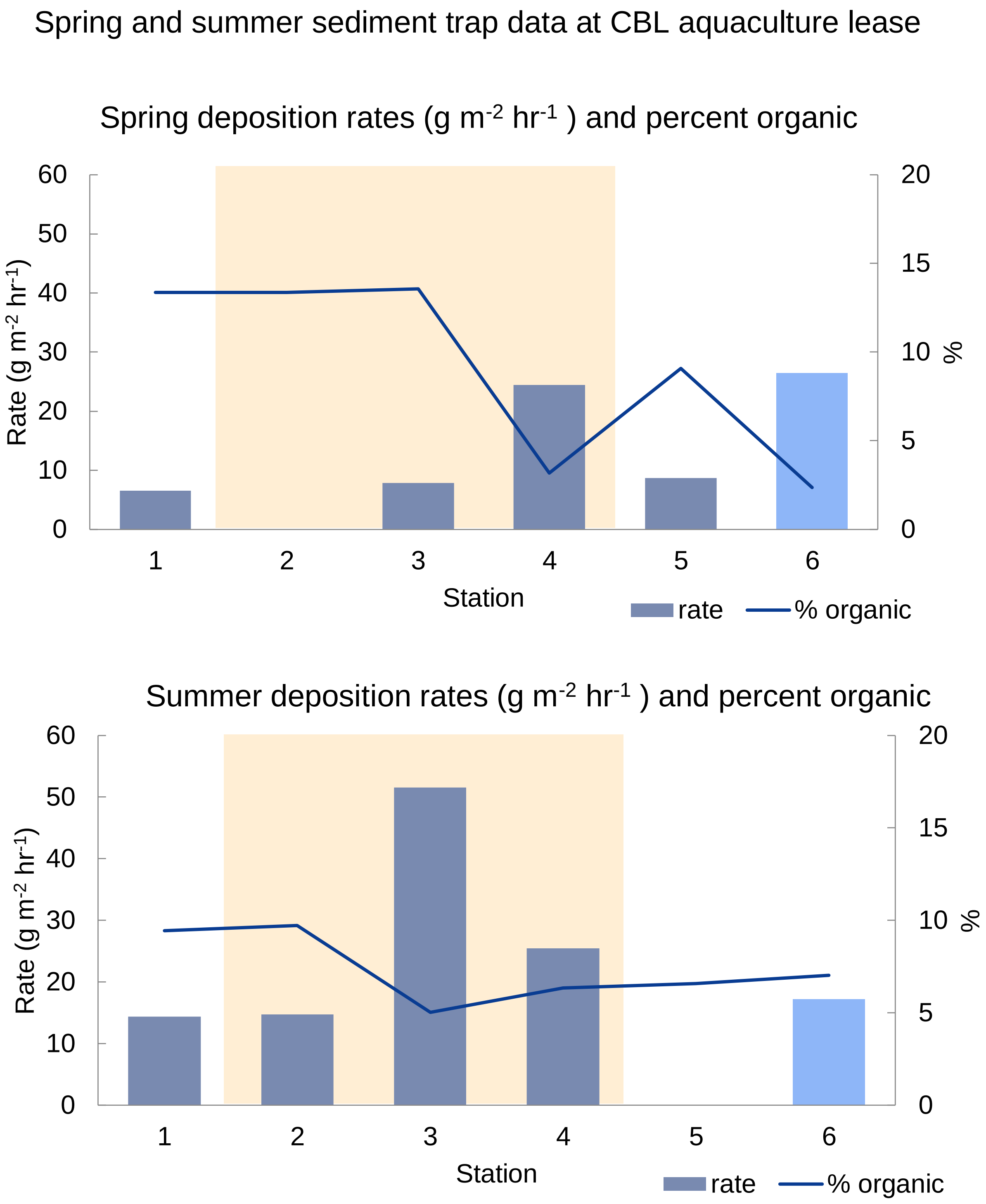

Figure 14. Sediment trap data from spring (top) and summer (bottom) deployments. Bar graphs show deposition rates (g m^{-2} hr^{-1}), and lines show the organic percentage. The shaded region denotes within farm stations 2, 3, and 4. Note the missing data for spring station 2 and summer station 5 (sediment trap knocked over).

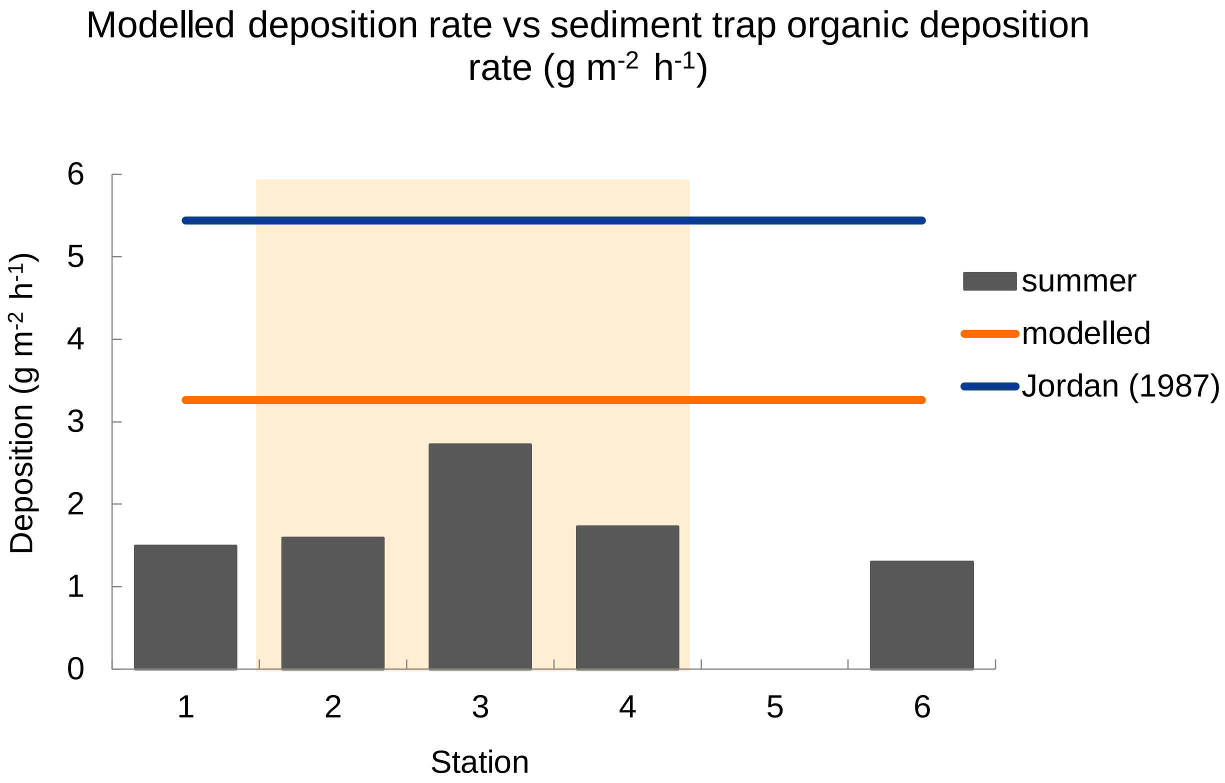

Figure 15. Summer sediment trap data of across farm organic deposition rates (bars; g m^{-2} hr^{-1}) plotted with mean biodeposition rates from the 2-week summer simulation using the bioenergetics model (orange line; 3.26 g m^{-2} hr^{-1}) and calculated using Jordan (1987) biodeposition formula (blue line; 5.44 g m^{-2} hr^{-1}). The shaded region denotes within farm stations 2, 3, and 4.

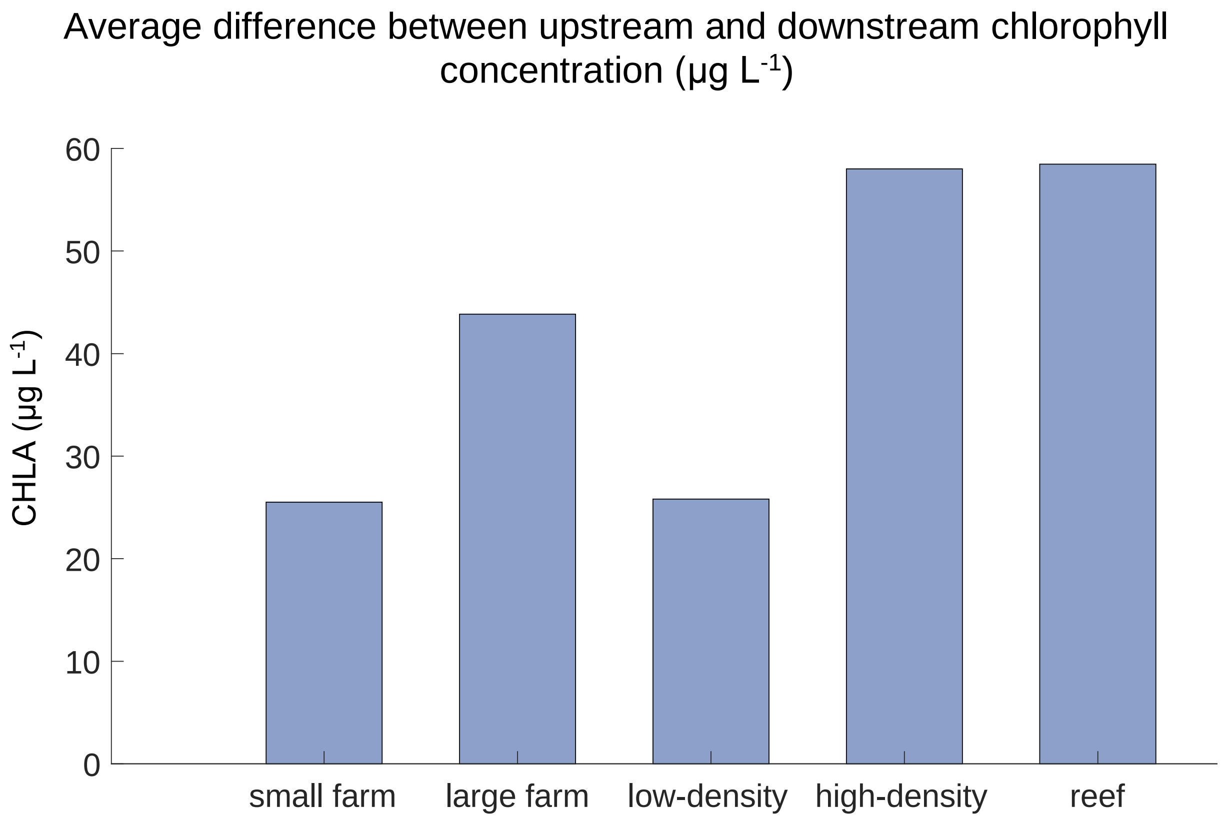

Figure 16. Difference in chlorophyll concentration (µg L^{-1}) between the first and last horizontal column of cells on the reef/farm domain. The upstream and downstream difference of each horizontal cell was calculated and summed for each model time step, and the average difference for each simulation is displayed.

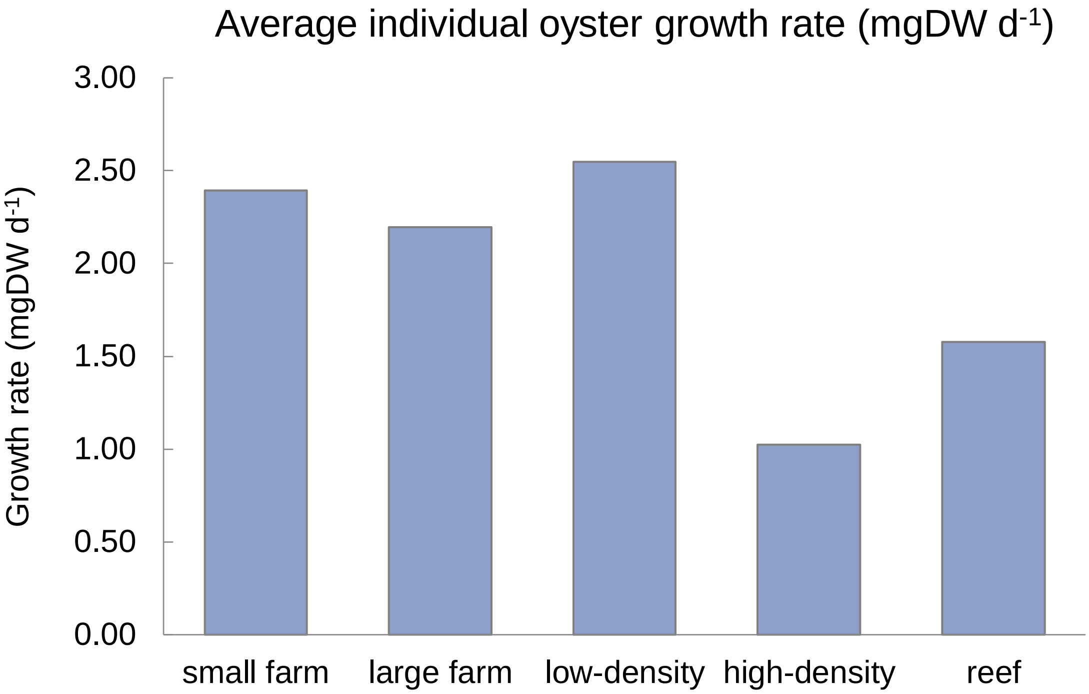

Figure 17. Individiual oyster growth rate (mgDW d^{-1}) averaged spatially across the reef and over the length of the simulation.

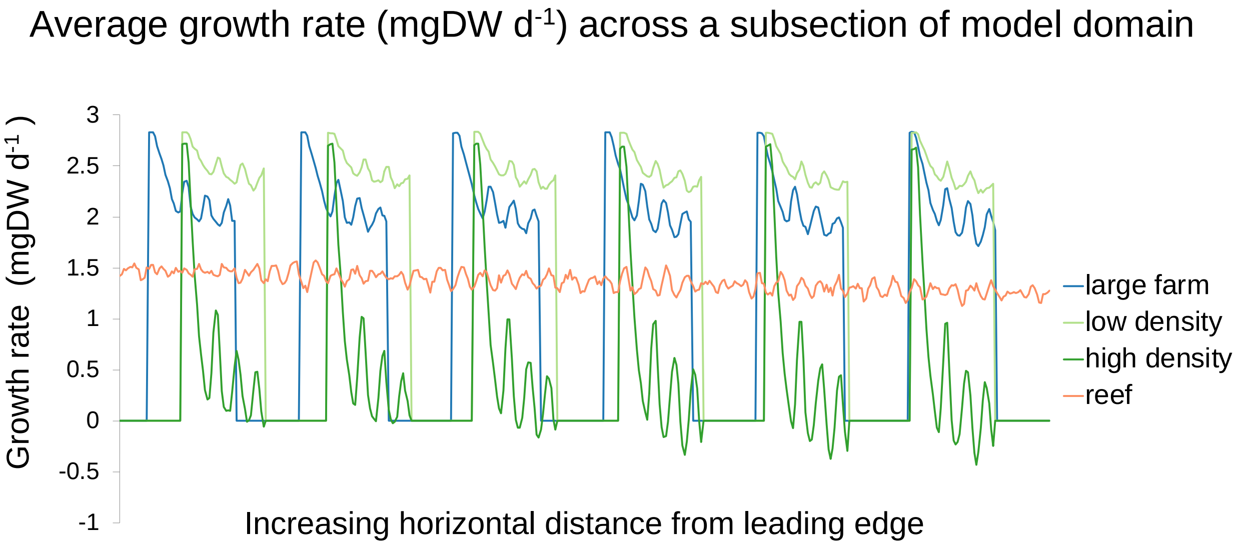

Figure 18. Oyster growth rate (mgDW d^{-1}) averaged over time across a subsection of model domain where growth rate on the high-density farm becomes negative for some oysters within a cage (begining ~35 m into the farm). The small farm is not included because is was 35 m long. Due to the spatial partitioning of the advection-diffusion and oyster bioenergetic subdomains, the size of a cell changes with reef/farm length. This figure shows ~450 cells representing 6 cages plus the spacing in between them. Because each cell ranges from ~2.3-2.9 cm in length, this figure shows a section of farm/reef approximately 10.4 to 13.05 m in length, depending on the simulation.. The reef is the only simulation with a continuous array of oysters, seen here a continuous function.

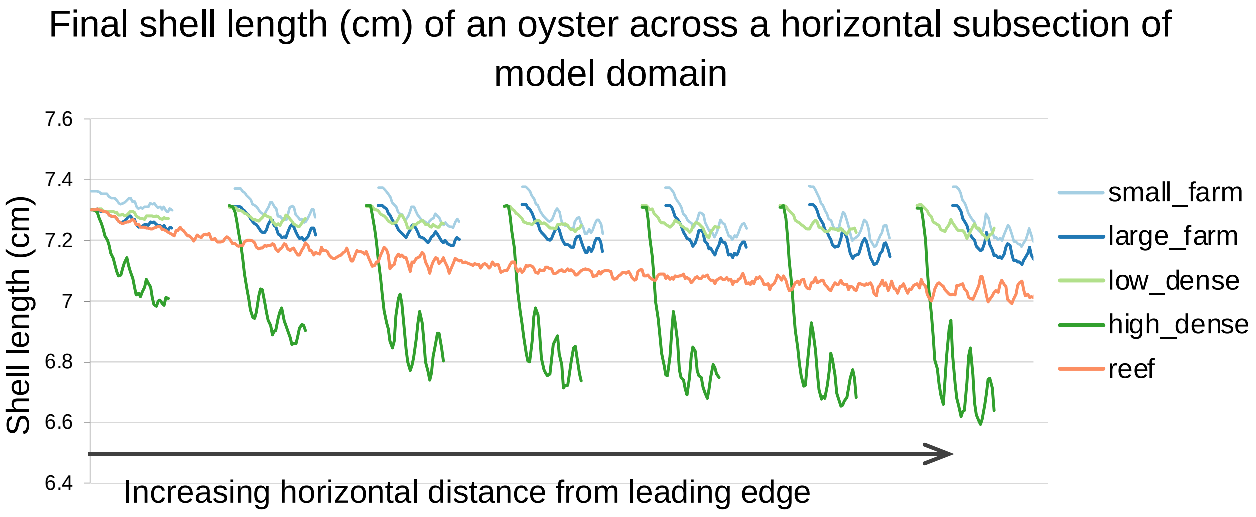

Figure 19. Final shell length of an oyster across a subsection of model domain begining at the leading edge of the farm/reef. Due to the spatial partitioning of the advection-diffusion and oyster bioenergetic subdomains, the size of a cell changes with reef/farm length. This figure shows 475 cells representing 7 cages and the spacing in between them. Because each cell ranges from ~2.3-2.9 cm in length, this figure shows the first 11.0 to 13.78 m of farm/reef, approximately, depending on the simulation. The reef is the only simulation with a continuous array of oysters, seen here a continuous function.

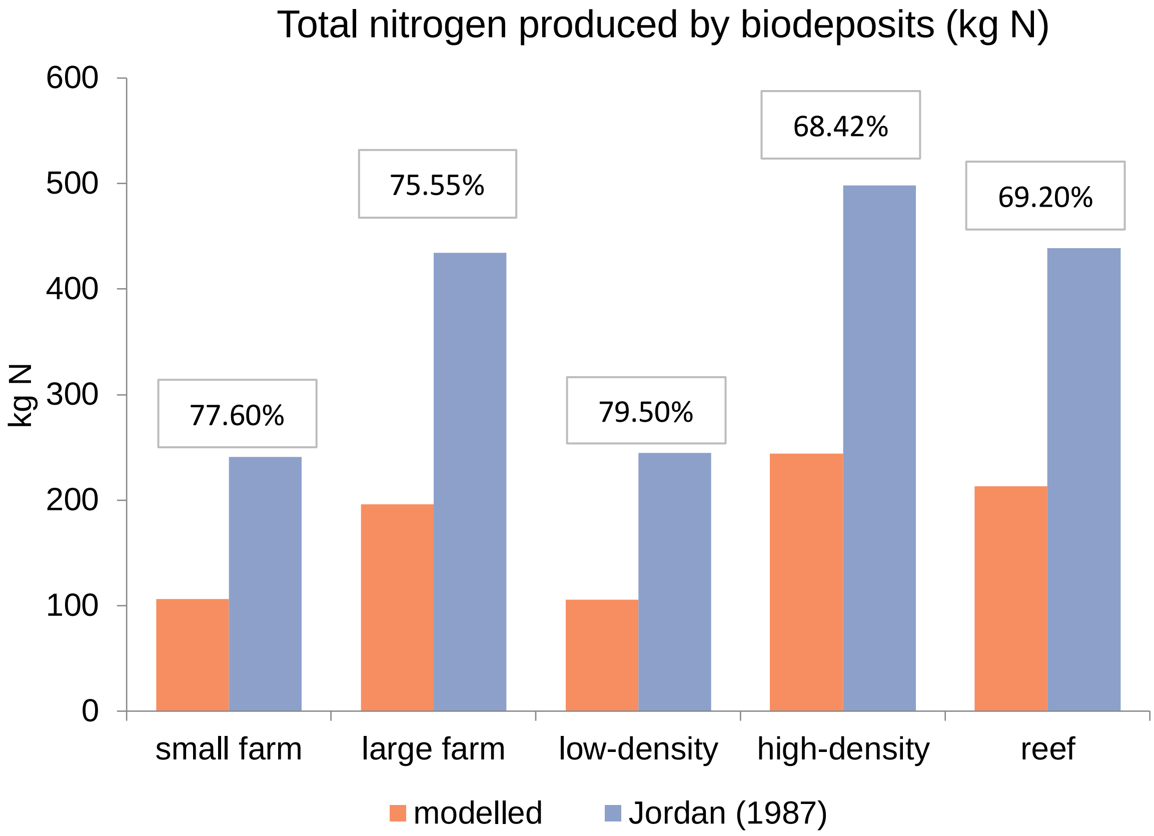

Figure 20. Total modelled biodeposit production (kg N) compared against biodeposit production calculated with the previous iteration of ReefBioDES (Jordan, 1987). Total deposition was calculated as the sum of biodeposits produced across the farm at each time step and then converted to grams of N using the same model conversion factors of 4.8 mg N per g biodeposits (Jordan, 1987). Percent difference between the two outputs is given for each simulation.

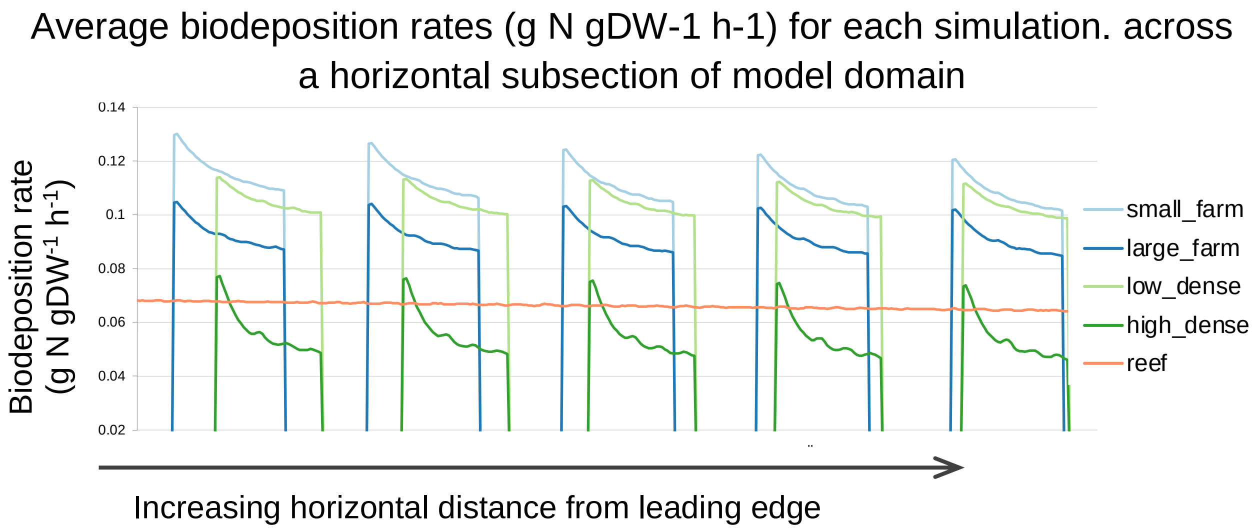

Figure 21. Along farm average biodeposition rates (g N gDW^{-1} h^{-1}) for each simulation. A mid-farm section approximately 6 cages in length is shown, where values were averaged over the duration of the simulations. Due to the spatial partitioning of the advection-diffusion and oyster bioenergetic subdomains, the size of a cell changes with reef/farm length. This figure shows 375 cells representing 5 cages plus the spacing in between them. Because each cell ranges from ~2.3-2.9 cm in length, this figure shows a section of farm/reef approximately 8.62 to 10.88 m in length. The reef is the only simulation with a continuous array of oysters, seen here a continuous function.

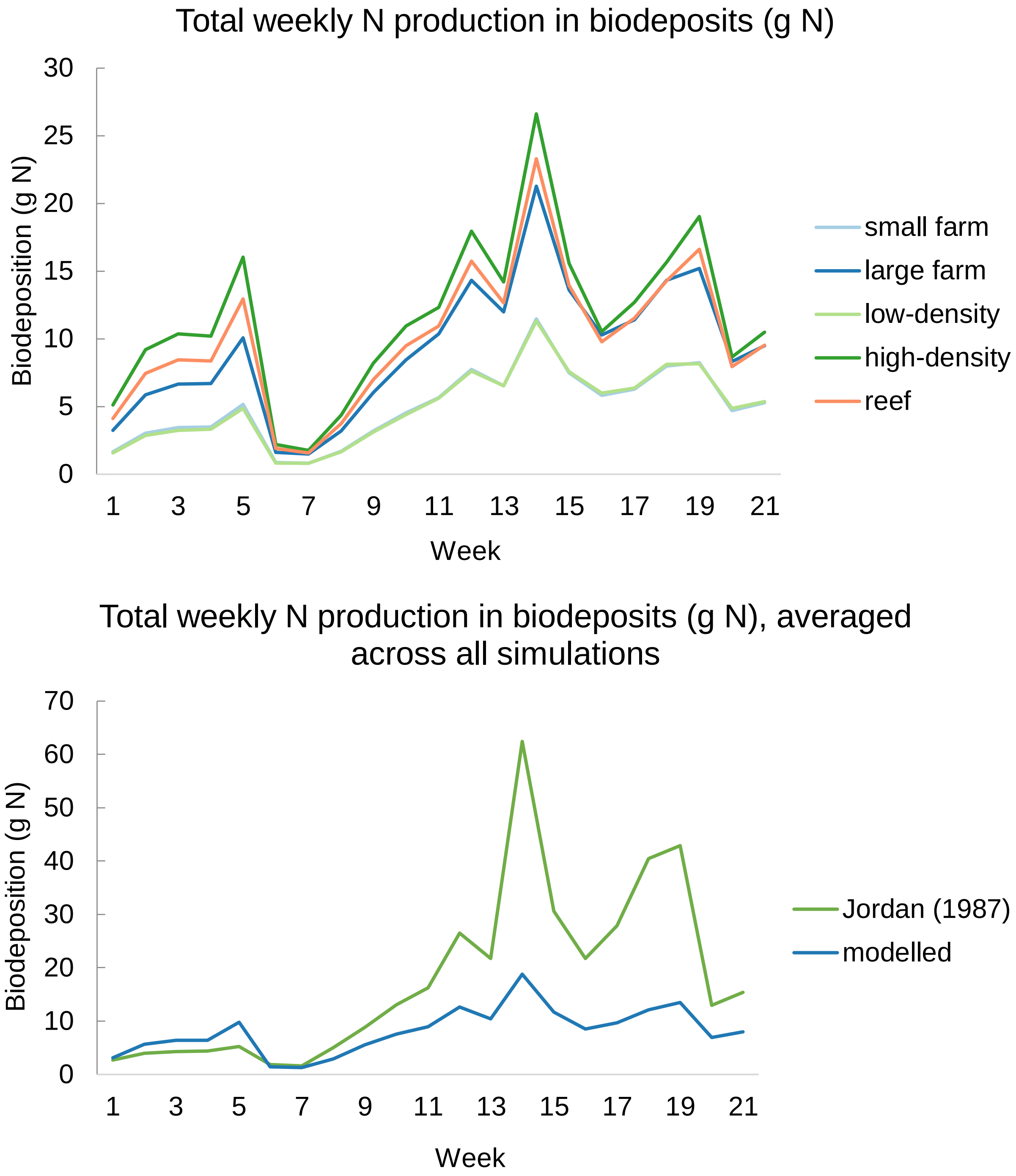

Figure 22. Trends of biodeposition (g N) averaged across the farm and summed for each week (top) biodeposit production using model formulations and (bottom) comparison of mean biodeposit production of all simulation using model formulation compared to using the Jordan (1987) formulation.

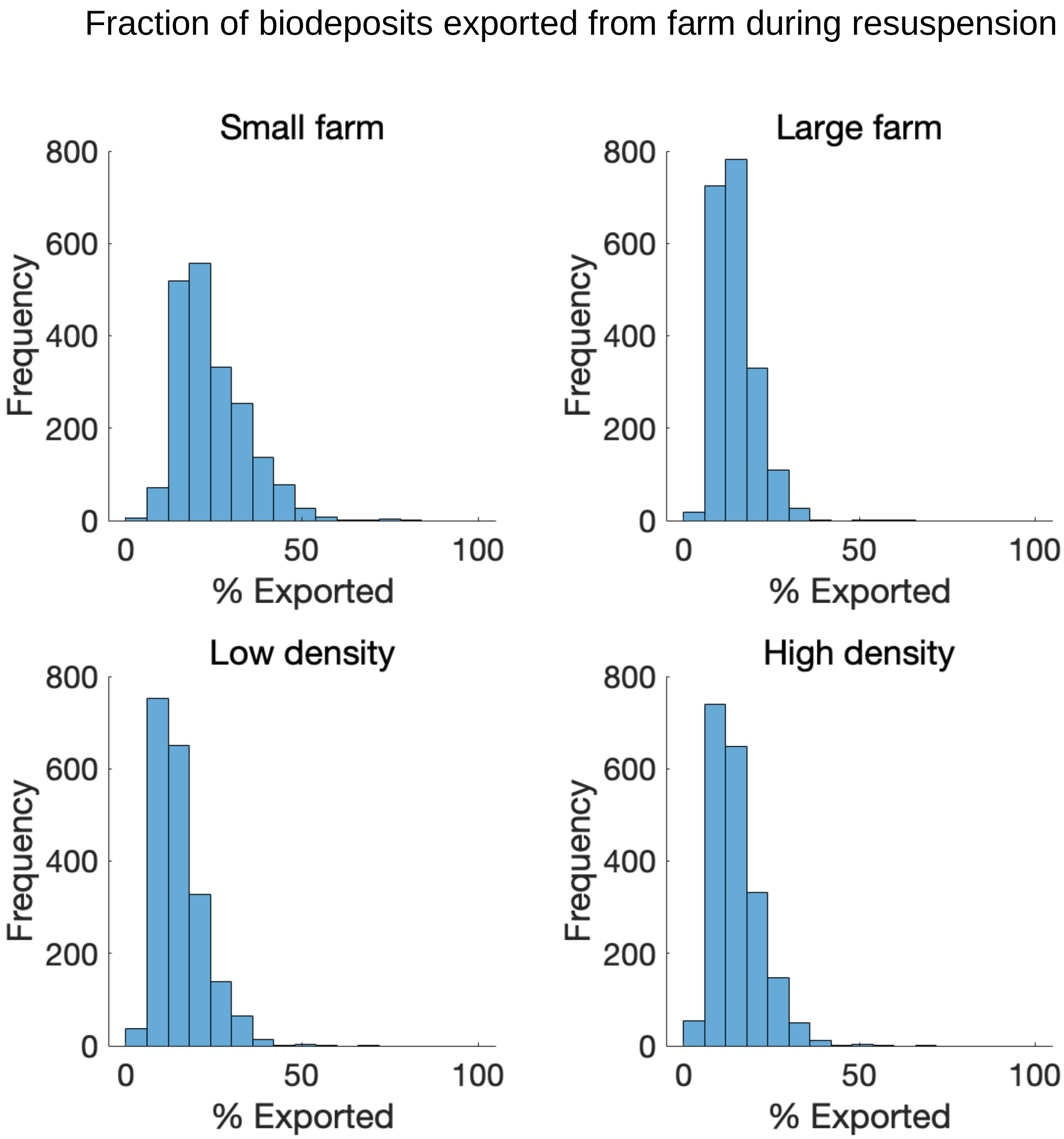

Figure 23. Comparison of biodeposit export during all farm simulations. Resuspension occurred in 55% of timesteps for all farm scenarios.

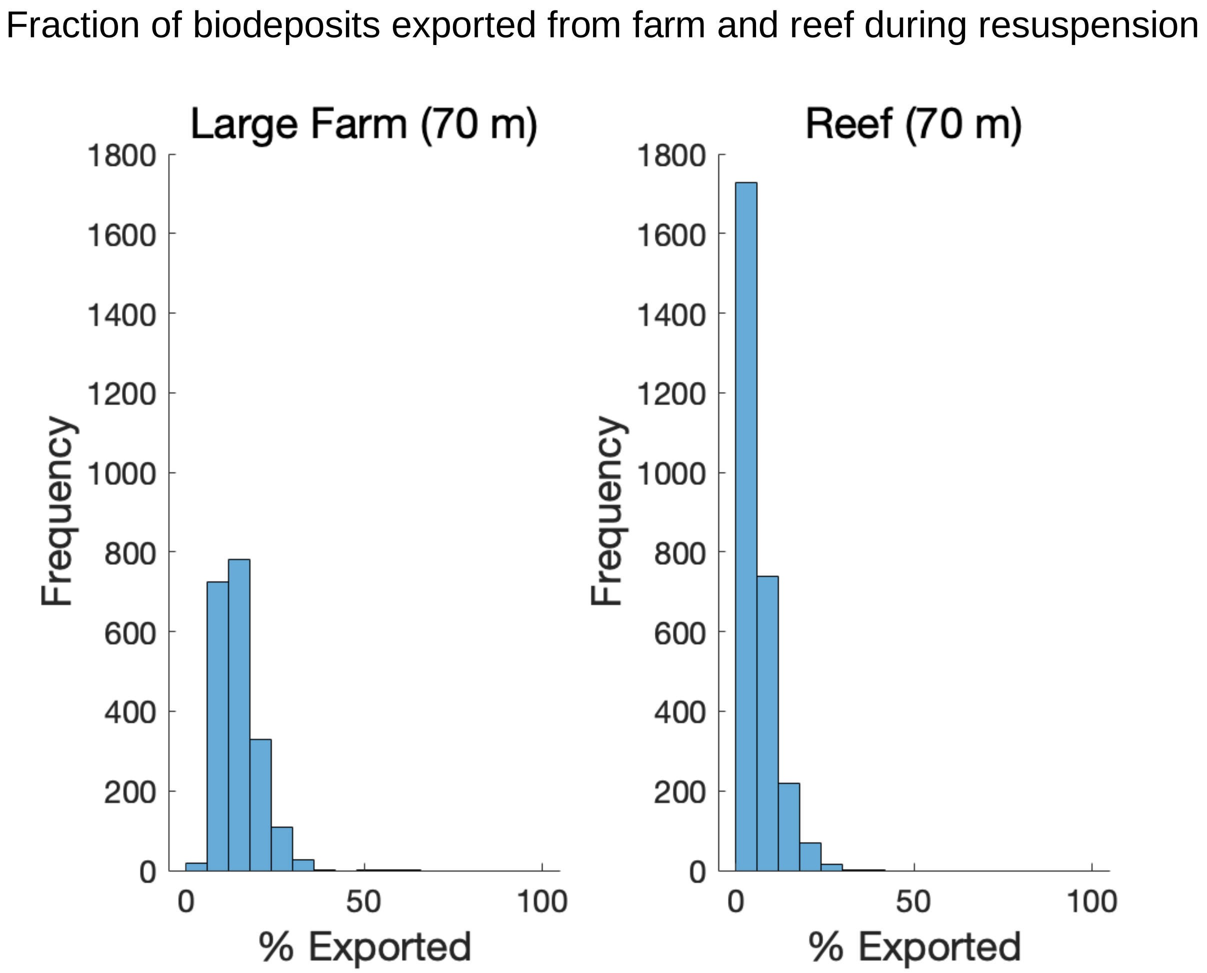

Figure 24. Comparison of biodeposit export between the large farm and reef simulation. Resuspension occurred in 55% of timesteps during the farm simulation and 76% of timesteps during the reef simulation.

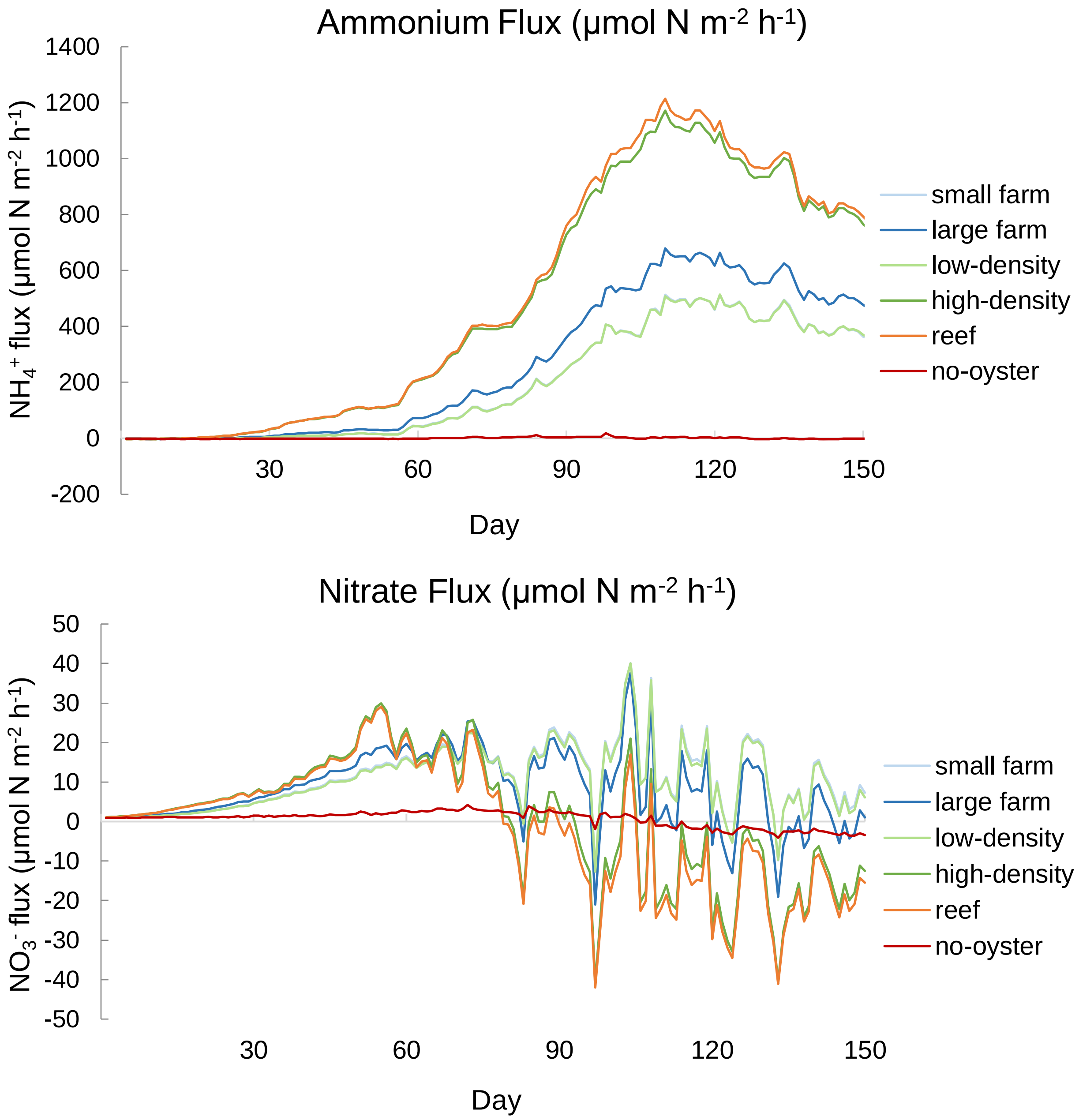

Figure 25. Sediment-water nitrogen fluxes for all simulations plotted with the reference no-oyster scenario for ammonium (top) and nitrate (bottom) fluxes (μmol m^{-2} h^{-1}). Note that the daily rates are almost identical for the small farm and low-density scenarios .

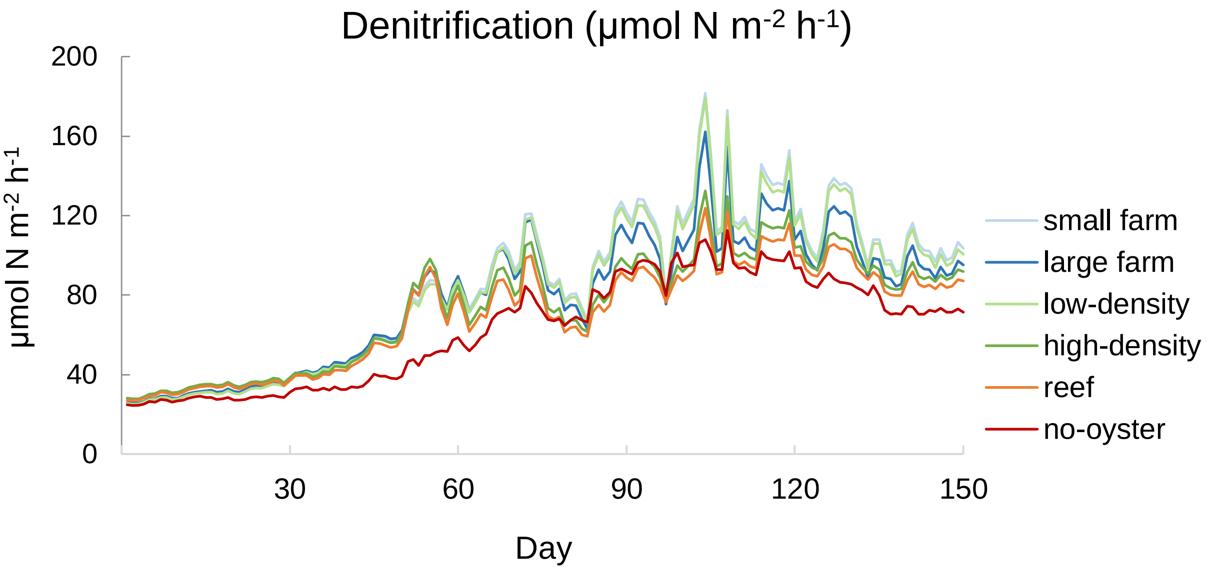

Figure 26. Denitrification rates (µmol m^{-2} h^{-1}) of all simulations plotted with the reference no-oyster scenario. Note that the daily rates are almost identical for the small farm and low-density scenarios .

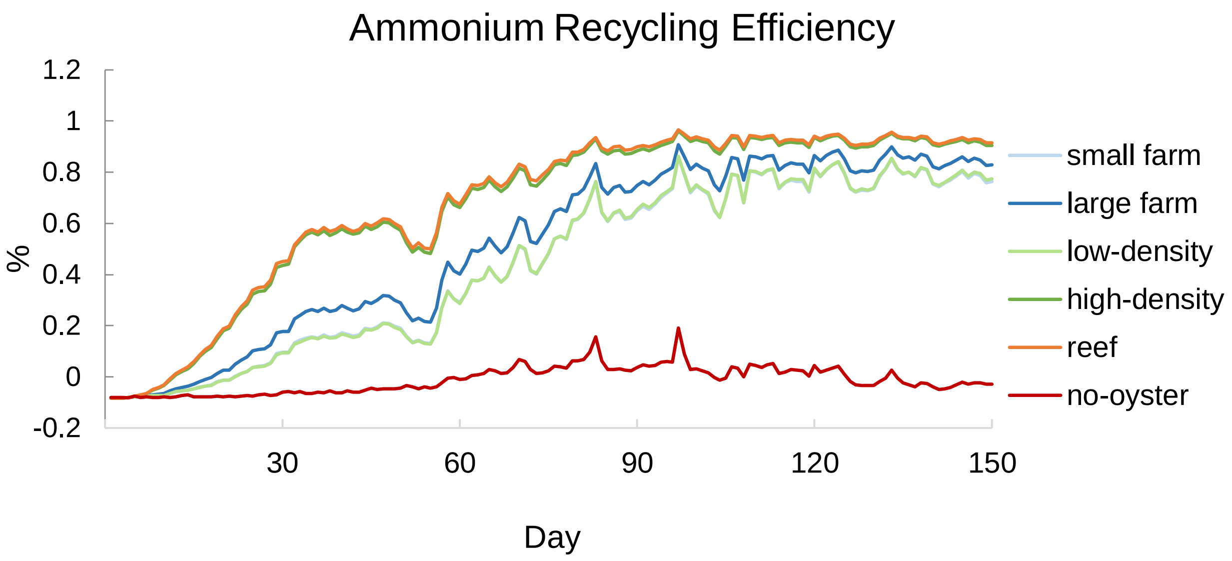

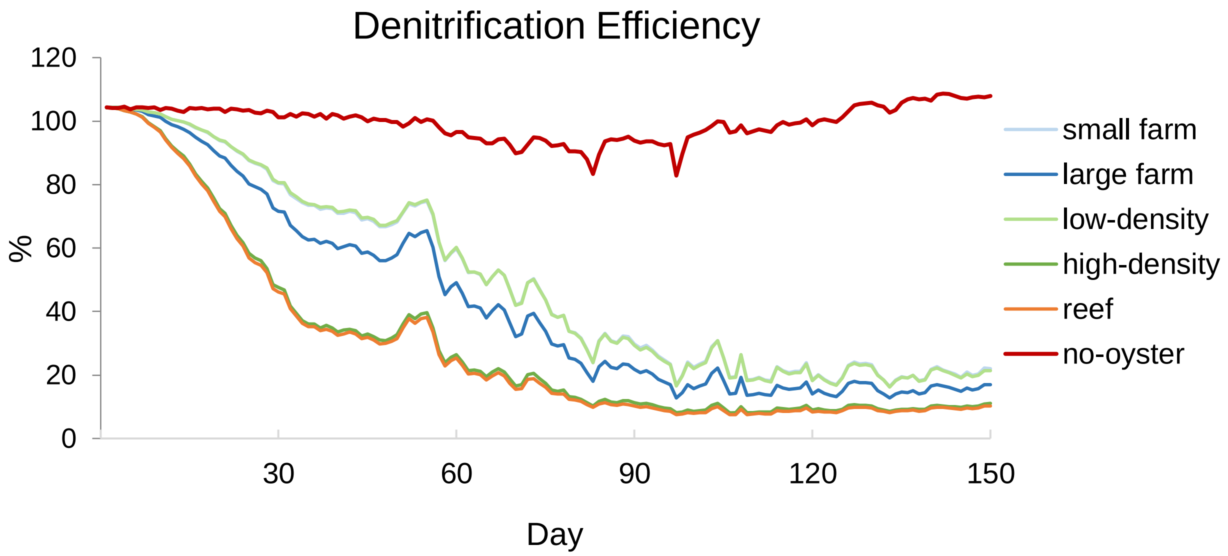

Figure 27. Ammonium recycling efficiencies (top) and denitrification efficiencies (bottom) for each day of the simulation.

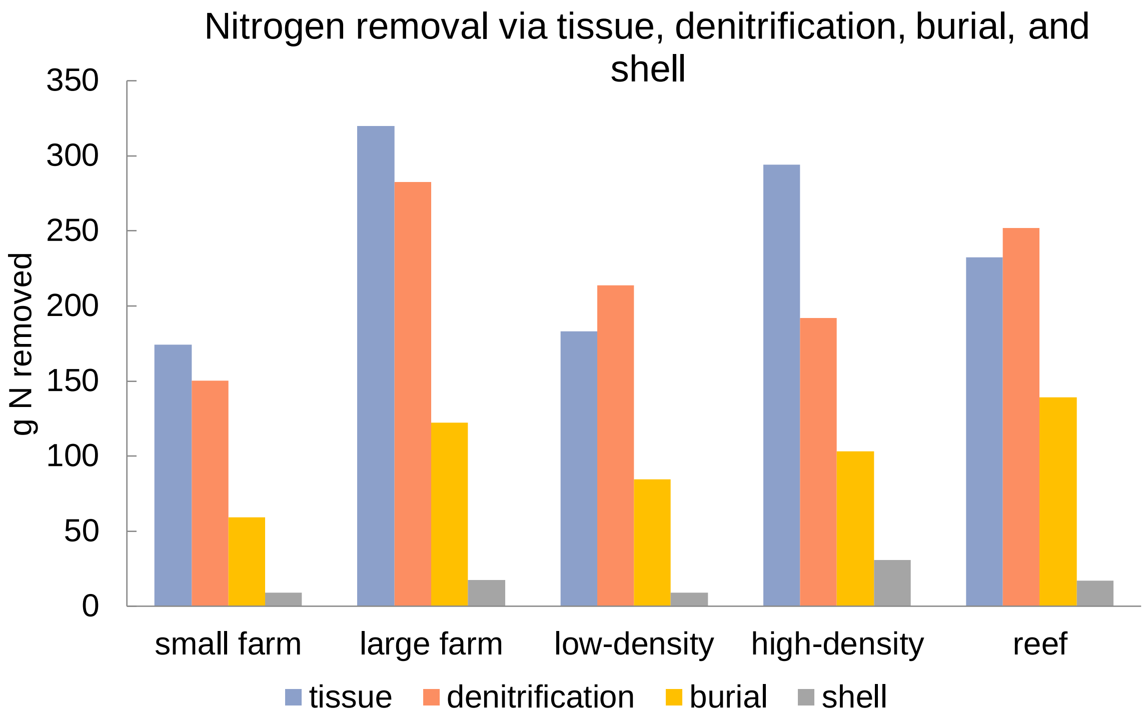

Figure 28. Grams of nitrogen removed via denitrification, burial, and tissue and shell accretion during the duration of the simulations (5 months). Tissue and shell N values were calculated only for the biomass that was acrued during the simulation.

References

Ayvazian, S., Mulvaney, K., Zarnoch, C., Palta, M., Reichert-Nguyen, J., McNally, S., Pilaro, M., Jones, A., Terry, C., & Fulweiler, R. W. (2021). Beyond Bioextraction: The Role of Oyster-Mediated Denitrification in Nutrient Management. *Environmental Science & Technology*, *55*(21), 14457–14465. https://doi.org/10.1021/acs.est.1c01901

Bi, C., & Xu, T. (2018). Numerical Study on the Flow Field Around a Fish Farm in Tidal Current. *Turkish Journal of Fisheries and Aquatic Sciences*, *18*, 705–716.

Bodenstein, S., Walton, W., & Steury, T. (2021). Effect of farming practices on growth and mortality rates in triploid and diploid eastern oysters Crassostrea virginica. *Aquaculture Environment Interactions*, *13*, 33–40. https://doi.org/10.3354/aei00387

Boyd, C. E. (2020). Eutrophication. In C. E. Boyd (Ed.), *Water Quality: An Introduction* (pp. 311–322). Springer International Publishing. https://doi.org/10.1007/978-3-030-23335-8_15

Burkholder, J., & Shumway, S. (2011). Bivalve Shellfish Aquaculture and Eutrophication. In *Shellfish Aquaculture and the Environment*. https://doi.org/10.1002/9780470960967.ch7

Butman, C. A., Fréchette, M., Geyer, W. R., & Starczak, V. R. (1994). Flume experiments on food supply to the blue mussel Mytilus edulis L. as a function of boundary-layerflow. *Limnology and Oceanography*, *39*(7), 1755–1768. https://doi.org/10.4319/lo.1994.39.7.1755

Caffrey, J. M., Hollibaugh, J. T., & Mortazavi, B. (2016). Living oysters and their shells as sites of nitrification and denitrification. *Marine Pollution Bulletin*, *112*(1), 86–90. https://doi.org/10.1016/j.marpolbul.2016.08.038

Campbell, M. D., & Hall, S. G. (2019). Hydrodynamic effects on oyster aquaculture systems: A review. *Reviews in Aquaculture, 11*(3), 896–906. https://doi.org/10.1111/raq.12271

Capelle, J. J., Hartog, E., Creemers, J., Heringa, J., & Kamermans, P. (2020). Effects of stocking density and immersion time on the performance of oysters in intertidal off-bottom culture. *Aquaculture International*, *28*(1), 249–264. https://doi.org/10.1007/s10499-019-00460-9

Cerco, C. F. (2015). A Multi-module Approach to Calculation of Oyster (Crassostrea virginica) Environmental Benefits. *Environmental Management*, *56*(2), 467–479. https://doi.org/10.1007/s00267-015-0511-3

Cerco, C. F., & Noel, M. R. (2005). *Evaluating ecosystem effects of oyster restoration in Chesapeake Bay* (Report of US Army Engineer Research and Development Center, Vicksburg MS).

Conley, D. J., Paerl, H. W., Howarth, R. W., Boesch, D. F., Seitzinger, S. P., Havens, K. E., Lancelot, C., & Likens, G. E. (2009). Controlling Eutrophication: Nitrogen and Phosphorus. *Science*, *323*(5917), 1014–1015. https://doi.org/10.1126/science.1167755

Cornwell, J., Rose, J., Kellogg, L., Luckenbach, M., Bricker, S., Paynter, K., Moore, C., Parker, M., Sanford, L., Wolinski, B., Lacatell, A., Fegley, L., & Hudson, K. (2016). *Panel Recommendations on the Oyster BMP Nutrient and Suspended Sediment Reduction Effectiveness Determination Decision Framework and Nitrogen and Phosphorus Assimilation in Oyster Tissue Reduction Effectiveness for Oyster Aquaculture Practices*. Chesapeake Bay Program (CBP).

Cranford, P., Hargrave, B. T., & Doucette, L. (2009). Benthic organic enrichment from suspended mussel (Mytilus edulis) culture in Prince Edward Island, Canada. *Aquaculture*, *292*, 189–196. https://doi.org/10.1016/j.aquaculture.2009.04.039

Dame, R. F. (2016). *Ecology of Marine Bivalves: An Ecosystem Approach* (2nd ed.). CRC Press. https://doi.org/10.1201/b11220

Denny, M. (1988). *Biology and the Mechanics of the Wave-Swept Environment*. Princeton University Press.

Diaz, R. J., & Rosenberg, R. (2008). Spreading Dead Zones and Consequences for Marine Ecosystems. *Science*, *321*(5891), 926–929. https://doi.org/10.1126/science.1156401

Duarte, P., Alvarez-Salgado, X. A., Fernández-Reiriz, M. J., Piedracoba, S., & Labarta, U. (2014). A modeling study on the hydrodynamics of a coastal embayment occupied by mussel farms (Ria de Ares-Betanzos, NW Iberian Peninsula). *Estuarine, Coastal and Shelf Science*, *147*, 42–55. https://doi.org/10.1016/j.ecss.2014.05.021

Dumbauld, B. R., Ruesink, J. L., & Rumrill, S. S. (2009). The ecological role of bivalve shellfish aquaculture in the estuarine environment: A review with application to oyster and clam culture in West Coast (USA) estuaries. *Aquaculture*, *290*(3), 196–223. https://doi.org/10.1016/j.aquaculture.2009.02.033

Ehrich, M. K., & Harris, L. A. (2015). A review of existing eastern oyster filtration rate models. *Ecological Modelling*, *297*, 201–212. https://doi.org/10.1016/j.ecolmodel.2014.11.023

Erbland, P. J., & Ozbay, G. (2008). A Comparison of the Macrofaunal Communities Inhabiting a Crassostrea virginica Oyster Reef and Oyster Aquaculture Gear in Indian River Bay, Delaware. *Journal of Shellfish Research*, *27*(4), 757–768. https://doi.org/10.2983/0730-8000(2008)27[757:ACOTMC]2.0.CO;2

Filgueira, R., Comeau, L. A., Landry, T., Grant, J., Guyondet, T., & Mallet, A. (2013). Bivalve condition index as an indicator of aquaculture intensity: A meta-analysis. *Ecological Indicators*, *25*, 215–229. https://doi.org/10.1016/j.ecolind.2012.10.001

Forsyth, M. (2014). *Investigations of the effects of oyster allometry and reef morphology on filtration rate and particle capture using numerical models* [M.S.]. University of Maryland.

Foster-Smith, R. L. (1975). The effect of concentration of suspension on the filtration rates and pseudofaecal production for Mytilus edulis L., Cerastoderma edule (L.) and Venerupis pullastra (Montagu). *Journal of Experimental Marine Biology and Ecology*, *17*(1), 1–22. https://doi.org/10.1016/0022-0981(75)90075-1

Fulford, R., Breitburg, D., Newell, R., Kemp, W., & Luckenbach, M. (2007). Effects of oyster population restoration strategies on phytoplankton biomass in Chesapeake Bay: A flexible modeling approach. *Marine Ecology Progress Series*, *336*, 43–61. https://doi.org/10.3354/meps336043

Glibert, P., Seitzinger, S., Heil, C., Burkholder, J., Parrow, M., Codispoti, L., & Kelly, V. (2005). The Role of Eutrophication in the Global Proliferation of Harmful Algal Blooms. *Oceanography*, *18*(2), 198–209. https://doi.org/10.5670/oceanog.2005.54

Hagy, J. D., Boynton, W. R., Keefe, C. W., & Wood, K. V. (2004). Hypoxia in Chesapeake Bay, 1950-2001: Long-Term Change in Relation to Nutrient Loading and River Flow. *Estuaries*, *27*(4), 634–658. JSTOR.

Harding, J. (2007). Comparison Of Growth Rates Between Diploid DEBY Eastern Oysters (Crassostrea Virginica, Gmelin 1791), Triploid Eastern Oysters, And Triploid Suminoe Oysters (C. Ariakensis, Fugita 1913). *Journal of Shellfish Research*, *26*(4), 961–972.

Haven, D. S., & Morales-Alamo, R. (1966). Aspects of biodeposition by oysters and other invertebrate filter feeders: Biodeposition by invertebrate filter feeders. *Limnology and Oceanography*, *11*(4), 487–498. https://doi.org/10.4319/lo.1966.11.4.0487

Hawkins, A. J. S., Pascoe, P. L., Parry, H., Brinsley, M., Black, K. D., McGonigle, C., Moore, H., Newell, C. R., O’Boyle, N., Ocarroll, T., O’Loan, B., Service, M., Smaal, A. C., Zhang, X. L., & Zhu, M. Y. (2013). Shellsim: A Generic Model of Growth and

Environmental Effects Validated Across Contrasting Habitats in Bivalve Shellfish. *Journal of Shellfish Research*, *32*(2), 237–253. https://doi.org/10.2983/035.032.0201

Higgins, C., Tobias, C., Piehler, M., Smyth, A., Dame, R., Stephenson, K., & Brown, B. (2013). Effect of aquacultured oyster biodeposition on sediment N-2 production in Chesapeake Bay. *Marine Ecology Progress Series*, *473*, 7–27. https://doi.org/10.3354/meps10062

Hoellein, T., Zarnoch, C., & Grizzle, R. (2015). Eastern oyster (Crassostrea virginica) filtration, biodeposition, and sediment nitrogen cycling at two oyster reefs with contrasting water quality in Great Bay Estuary (New Hampshire, USA). *Biogeochemistry*, *122*. https://doi.org/10.1007/s10533-014-0034-7

Holyoke, R. (2008). *Biodeposition and biogeochemical processes in shallow, mesohaline sediments of Chesapeake Bay* [Ph.D.]. Univesity of Maryland.

Humphries, A. T., Ayvazian, S. G., Carey, J. C., Hancock, B. T., Grabbert, S., Cobb, D., Strobel, C. J., & Fulweiler, R. W. (2016). Directly Measured Denitrification Reveals Oyster Aquaculture and Restored Oyster Reefs Remove Nitrogen at Comparable High Rates. *Frontiers in Marine Science*, *3*, 74. https://doi.org/10.3389/fmars.2016.00074

Jenkins, M. C., & Kemp, W. M. (1984). The coupling of nitrification and denitrification in two estuarine sediments1,2: Nitrification-denitrification. *Limnology and Oceanography*, *29*(3), 609–619. https://doi.org/10.4319/lo.1984.29.3.0609

Jones, C., Branosky, E., Selman, M., & Perez, M. (2010). *How Nutrient Trading Could Help Restore the Chesapeake Bay*.

Jordan, S. J. (1987). *Sedimentation and Remineralization Associated with Biodeposition by the American Oyster Crassostrea Virginica (Gmelin)*. University of Maryland, College Park.

Jørgensen, B. B. (1977). Bacterial sulfate reduction within reduced microniches of oxidized marine sediments. *Marine Biology*, *41*, 7–17.

Kahover, K. (2022). *Using a high resolution, mechanistic model of filtration, biodeposition, hydrodynamics, and sediment biodgeochemistry in order to understand the driving forces behind nitrogen dynamics on oyster reefs* [M.S.]. University of Maryland.

Kellogg, M., Cornwell, J., Owens, M., & Paynter, K. (2013). Denitrification and nutrient assimilation on a restored oyster reef. *Marine Ecology Progress Series*, *480*, 1–19. https://doi.org/10.3354/meps10331

Kellogg, M. L., Brush, M. J., & Cornwell, J. (2018). *An updated model for estimating the TMDL-related benefits of oyster reef restoration Harris Creek, Maryland, USA*. https://doi.org/10.25773/7A75-DS48

Kellogg, M. L., Smyth, A. R., Luckenbach, M. W., Carmichael, R. H., Brown, B. L., Cornwell, J. C., Piehler, M. F., Owens, M. S., Dalrymple, D. J., & Higgins, C. B. (2014). Use of oysters to mitigate eutrophication in coastal waters. *Estuarine, Coastal and Shelf Science*, *151*, 156–168. https://doi.org/10.1016/j.ecss.2014.09.025

Kemp, M., Boynton, W. R., J. E. Adolf, D. F. Boesch, W. C. Boicourt, G. Brush, J. C. Cornwell, T. R. Fisher, P. M. Glibert, J. D. Hagy, L. W. Harding, E. D. Houde, D. G. Kimmel, W. D. Miller, R. I. E. Newell, M. R. Roman, E. M. Smith, & J. C. Stevenson. (2005). Eutrophication of Chesapeake Bay: Historical trends and ecological interactions. *Marine Ecology Progress Series*, *303*, 1–29.

Lavaud, R., La Peyre, M. K., Casas, S. M., Bacher, C., & La Peyre, J. F. (2017). Integrating the effects of salinity on the physiology of the eastern oyster, Crassostrea virginica, in the northern Gulf of Mexico through a Dynamic Energy Budget model. *Ecological Modelling*, *363*, 221–233. https://doi.org/10.1016/j.ecolmodel.2017.09.003

Lettau, H. (1969). Note on Aerodynamic Roughness-Parameter Estimation on the Basis of Roughness-Element Description. *Journal of Applied Meteorology (1962-1982)*, *8*(5), 828–832. JSTOR.

Lunstrum, A., McGlathery, K., & Smyth, A. (2018). Oyster (Crassostrea virginica) Aquaculture Shifts Sediment Nitrogen Processes toward Mineralization over Denitrification. *Estuaries and Coasts*, *41*(4), 1130–1146. https://doi.org/10.1007/s12237-017-0327-x

Marenghi, F., Ozbay, G., Erbland, P., & Rossi-Snook, K. (2010). A comparison of the habitat value of sub-tidal and floating oyster (Crassostrea virginica) aquaculture gear with a created reef in Delaware’s Inland Bays, USA. *Aquaculture International*, *18*(1), 69–81. https://doi.org/10.1007/s10499-009-9273-3

Mazouni, N., Gaertner, J.-C., Deslous-Paoli, J.-M., Landrein, S., & Geringer d’Oedenberg, M. (1996). Nutrient and oxygen exchanges at the water–sediment interface in a shellfish farming lagoon (Thau, France). *Journal of Experimental Marine Biology and Ecology*, *205*(1), 91–113. https://doi.org/10.1016/S0022-0981(96)02594-4

Mercaldo-Allen, R., Clark, P., Liu, Y., Phillips, G., Redman, D., Auster, P., Estela, E., Milke, L., Verkade, A., & Rose, J. (2021). Exploring video and eDNA metabarcoding methods to assess oyster aquaculture cages as fish habitat. *Aquaculture Environment Interactions*, *13*, 277–294. https://doi.org/10.3354/aei00408

Newell, R. I. (1996). Mechanisms and physiology of larval and adult feeding. *The Eastern Oyster Crassostrea Virginica*.

Newell, R. I. E., Fisher, T. R., Holyoke, R. R., & Cornwell, J. C. (2005). Influence of Eastern Oysters on Nitrogen and Phosphorus Regeneration in Chesapeake Bay, USA. In R. F. Dame & S. Olenin (Eds.), *The Comparative Roles of Suspension-Feeders in Ecosystems* (Vol. 47, pp. 93–120). Springer-Verlag. https://doi.org/10.1007/1-4020-3030-4_6

Newell, R., & Jordan, S. (1983). Preferential ingestion of organic material by the American oyster Crassostrea virginica. *Marine Ecology Progress Series*, *13*, 47–53. https://doi.org/10.3354/meps013047

Powell, E. N., Hofmann, E. E., Klinck, J. M., & Ray, S. M. (1992). *Modeling oyster populations: I. A commentary on filtration rate. Is faster always better?*

Raupach, M. R. (1992). Drag and drag partition on rough surfaces. *Boundary-Layer Meteorology*, *60*(4), 375–395. https://doi.org/10.1007/BF00155203

Ray, N. E., & Fulweiler, R. W. (2021). Meta-analysis of oyster impacts on coastal biogeochemistry. *Nature Sustainability*, *4*(3), 261–269. https://doi.org/10.1038/s41893-020-00644-9

Reidenbach, M. A., Berg, P., Hume, A., Hansen, J. C. R., & Whitman, E. R. (2013). Hydrodynamics of intertidal oyster reefs: The influence of boundary layer flow processes on sediment and oxygen exchange: Oyster reef sediment and oxygen exchange. *Limnology and Oceanography: Fluids and Environments*, *3*(1), 225–239. https://doi.org/10.1215/21573689-2395266

Ring, C. (2012). *Evaluation of a Mechanical Grader for the Improvement of the Aquaculture Production of the Eastern Oyster, Crassostrea virginica, in the Northern Gulf of Mexico* [Thesis]. https://etd.auburn.edu//handle/10415/2953

Rose, J. M., Gosnell, J. S., Bricker, S., Brush, M. J., Colden, A., Harris, L., Karplus, E., Laferriere, A., Merrill, N. H., Murphy, T. B., Reitsma, J., Shockley, J., Stephenson, K., Theuerkauf, S., Ward, D., & Fulweiler, R. W. (2021). Opportunities and Challenges for Including Oyster-Mediated Denitrification in Nitrogen Management Plans. *Estuaries and Coasts*, *44*(8), 2041–2055. https://doi.org/10.1007/s12237-021-00936-z

Shao, Y., & Yang, Y. (2005). A scheme for drag partition over rough surfaces. *Atmospheric Environment*, *39*(38), 7351–7361. https://doi.org/10.1016/j.atmosenv.2005.09.014

Stephenson, K., & Shabman, L. (2017a). Nutrient Assimilation Services for Water Quality Credit Trading Programs: A Comparative Analysis with Nonpoint Source Credits. *Coastal Management*, *45*(1), 24–43. https://doi.org/10.1080/08920753.2017.1237240

Stephenson, K., & Shabman, L. (2017b). Can Water Quality Trading Fix the Agricultural Nonpoint Source Problem? *Annual Review of Resource Economics*, *9*(1), 95–116. https://doi.org/10.1146/annurev-resource-100516-053639

Styles, R. (2015). Flow and Turbulence over an Oyster Reef. *Journal of Coastal Research*, *31*(4), 978–985. https://doi.org/10.2112/JCOASTRES-D-14-00115.1

Tenore, K. R. (1988). *Changes in composition and nutritional value to a benthic deposit feeder of decomposing detritus pools*.

Tenore, K. R., & Dunstan, W. M. (1973). Comparison of feeding and biodeposition of three bivalves at different food levels. *Marine Biology*, *21*(3), 190–195. https://doi.org/10.1007/BF00355249

Testa, J., Brady, D., Cornwell, J., Owens, M., Sanford, L., Newell, C., Suttles, S., & Newell, R. (2015). Modeling the impact of floating oyster (Crassostrea virginica) aquaculture on sediment-water nutrient and oxygen fluxes. *Aquaculture Environment Interactions*, *7*(3), 205–222. https://doi.org/10.3354/aei00151

Testa, J. M., Brady, D. C., Di Toro, D. M., Boynton, W. R., Cornwell, J. C., & Kemp, W. M. (2013). Sediment flux modeling: Simulating nitrogen, phosphorus, and silica cycles. *Estuarine, Coastal and Shelf Science*, *131*, 245–263. https://doi.org/10.1016/j.ecss.2013.06.014

Theurer, W. (1973). *Dispersion of ground-level emissions in complex built-up areas* [Ph.D.]. University of Maryland.

Van Senten, J., Engle, C., Parker, M., & Webster, D. (2019). *Analysis of the Economic Benefits of the Maryland Shellfish Aquaculture Industry*. Chesapeake Bay Foundation (CBF).

Ward, E., & Shumway, S. (2004). Separating the grain from the chaff: Particle selection in suspension- and deposit-feeding bivalves. *VOLUME 300 Special Issue*, *300*(1), 83–130. https://doi.org/10.1016/j.jembe.2004.03.002

Weissberger, E. J., & Glibert, P. M. (2021). Diet of the eastern oyster, Crassostrea virginica, growing in a eutrophic tributary of Chesapeake Bay, Maryland, USA. *Aquaculture Reports*, *20*, 100655. https://doi.org/10.1016/j.aqrep.2021.100655

Wu, Y., Chaffey, J., Law, B. A., Greenberg, D. A., Drozdowski, A., Page, F. H., & Haigh, S. P. (2014). A three-dimensional hydrodynamic model for aquaculture: A case study in the Bay of Fundy. *Aquaculture Environment Interactions*, *5*, 235–248.

Zhao, Y.-P., Bi, C.-W., Chen, C.-P., Li, Y.-C., & Dong, G.-H. (2015). Experimental study on flow velocity and mooring loads for multiple net cages in steady current. *Aquacultural Engineering*, *67*, 24–31. https://doi.org/10.1016/j.aquaeng.2015.05.005